Chandra Large Project observations of the supernova remnant N132D: measuring the expansion of the forward shock

Long, X.; Plucinsky, P.P.; Gaetz, T.J.; Kashyap, V.L.; Bamba, A.; Blair, W.P.; ... ; Yamaguchi, H.

The Astrophysical Journal, 993:136 (24pp), 2025 November 1 https://doi.org/10.3847/1538-4357/ae07c7

Chandra Large Project Observations of the Supernova Remnant N132D: Measuring the Expansion of the Forward Shock

Xi Long[1,2], Paul P. Plucinsky[2], Terrance J. Gaetz[2], Vinay L. Kashyap[2], Aya Bamba[3,4,5], William P. Blair[6], Daniel Castro[2], Adam R. Foster[2], Charles J. Law[7,18], Dan Milisavljevic[8,9], Eric Miller[10], Daniel J. Patnaude[2], Manami Sasaki[11], Hidetoshi Sano[12,13], Piyush Sharda[14], Benjamin F. Williams[15], Brian J. Williams[16], and Hiroya Yamaguchi[17]

[1] Department of Physics, The University of Hong Kong, Pokfulam Road, Hong Kong
[2] Center for Astrophysics | Harvard & Smithsonian, 60 Garden Street, Cambridge, MA 02138, USA
[3] Department of Physics, Graduate School of Science, The University of Tokyo, 7-3-1 Hongo, Bunkyo-ku, Tokyo 113-0033, Japan
[4] Research Center for the Early Universe, School of Science, The University of Tokyo, 7-3-1 Hongo, Bunkyo-ku, Tokyo 113-0033, Japan
[5] Trans-Scale Quantum Science Institute, The University of Tokyo, Tokyo 113-0033, Japan
[6] The William H. Miller III Department of Physics and Astronomy, Johns Hopkins University, 3400 North Charles Street, Baltimore, MD 21218, USA
[7] Department of Astronomy, University of Virginia, Charlottesville, VA 22904, USA
[8] Purdue University, Department of Physics and Astronomy, 525 Northwestern Avenue, West Lafayette, IN 47907, USA
[9] Integrative Data Science Initiative, Purdue University, West Lafayette, IN 47907, USA
[10] Kavli Institute for Astrophysics and Space Research, Massachusetts Institute of Technology, Cambridge, MA 02139, USA
[11] Dr. Karl Remeis Observatory, Erlangen Centre for Astroparticle Physics, Friedrich-Alexander-Universität Erlangen-Nürnberg, Sternwartstraße 7, 96049 Bamberg, Germany
[12] Faculty of Engineering, Gifu University, 1-1 Yanagido, Gifu 501-1193, Japan
[13] Center for Space Research and Utilization Promotion (c-SRUP), Gifu University, 1-1 Yanagido, Gifu 501-1193, Japan
[14] Leiden Observatory, Leiden University, PO Box 9513, NL-2300 RA Leiden, The Netherlands
[15] Department of Astronomy, University of Washington, Box 351580, Seattle, WA 98195, USA
[16] NASA Goddard Space Flight Center, Code 662, Greenbelt, MD 20771, USA
[17] ISAS/JAXA, 3-1-1 Yoshinodai, Chuo-ku, Sagamihara, Kanagawa 252-5210, Japan
Received 2025 July 1; revised 2025 September 13; accepted 2025 September 15; published 2025 October 29

Abstract

We present results from the Chandra X-ray Observatory Large Project (878 ks in 28 observations) of the Large Magellanic Cloud supernova remnant N132D. We measure the expansion of the forward shock in the bright southern rim to be $0\farcs10 \pm 0\farcs02$ over the ∼14.5 yr baseline, which corresponds to a velocity of $1620 \pm 400\,\mathrm{km\,s^{-1}}$ after accounting for several instrumental effects. We measure an expansion of $0\farcs23 \pm 0\farcs02$ and a shock velocity of $3840 \pm 260\,\mathrm{km\,s^{-1}}$ for two features in an apparent blowout region in the northeast. The emission-measure-weighted average temperature inferred from X-ray spectral fits to regions in the southern rim is 0.95 ± 0.17 keV, consistent with the electron temperature implied by the shock velocity after accounting for Coulomb equilibration and adiabatic expansion. In contrast, the emission-measure-weighted average temperature for the northeast region is 0.77 ± 0.04 keV, which is significantly lower than the value inferred from the shock velocity. We fit 1D evolutionary models for the shock in the southern rim and northeast region, using the measured radius and propagation velocity into constant density and power-law profile circumstellar media. We find good agreement with the age of ∼2500 yr derived from optical expansion measurements for explosion energies of 1.5–3.0 × 10^{51} erg, ejecta masses of 2–6 $M_{\odot}$, and ambient medium densities of ∼0.33–0.66 amu $\mathrm{cm^{-3}}$ in the south and ∼0.01–0.02 amu $\mathrm{cm^{-3}}$ in the northeast assuming a constant density medium. These results are consistent with previous studies that suggested the progenitor of N132D was an energetic supernova that exploded into a preexisting cavity.

Unified Astronomy Thesaurus concepts: Supernova remnants (1667); Interstellar medium (847); Plasma astrophysics (1261)

1. Introduction

Massive stars and their supernovae (SNe) are important contributors to the structure and evolution of the interstellar medium (ISM; D. P. Cox & B. W. Smith 1974; C. F. McKee & J. P. Ostriker 1977; M. S. Oey 1996; S. Silich et al. 2005; F. A. Gent et al. 2013; C.-G. Kim & E. C. Ostriker 2015, 2017; K. El-Badry et al. 2019) and determine the chemical evolution of galaxies (C. Kobayashi et al. 2006; K. Nomoto et al. 2013). They are the dominant sources of the warm and hot ionized gas in the ISM and a significant contributor to the turbulence in the ISM (M. de Avillez & D. Breitschwerdt 2004; M. K. R. Joung & M.-M. Mac Low 2006). In addition, most of the metals in the Universe are produced by nucleosynthesis in massive stars (K. Nomoto et al. 2006; T. Sukhbold et al. 2016) and these products are distributed throughout the ISM by SNe and SN remnants (SNRs; J. P. Hughes et al. 2000; J. Bhalerao et al. 2019).

Massive stars form in dense clumps in molecular cloud (MC) complexes or OB associations (H. Zinnecker & H. W. Yorke 2007; S. Pfalzner et al. 2012; J. L. Ward & J. M. D. Kruijssen 2018) as shown in surveys of star-forming regions in the Milky Way (F. Motte et al. 2018;

[18] NASA Hubble Fellowship Program Sagan Fellow.

T. Cantat-Gaudin 2022). The winds of massive stars may be powerful enough to excavate a cavity in the MC complex over the lifetime of the star (C. F. McKee et al. 1984; V. V. Dwarkadas 2023), producing a region of low-density, ionized or partially ionized gas surrounded by a denser, neutral shell of material. Stars more massive than 8 $M_{\odot}$ will end their lives as core-collapse SNe (CCSNe) or directly collapse to a black hole (A. Heger et al. 2003). Given the relatively short lifetimes of these massive stars, it is likely that the star will be close to the MC in which it formed at the time of explosion (R. A. Chevalier 1999; P. Slane et al. 2016; N. J. Wright 2020).

After the star explodes, the expanding shock from the SN will propagate through the relatively low-density material in the cavity before encountering denser material at the edge of the cavity (R. A. Chevalier & E. P. Liang 1989; G. Tenorio-Tagle et al. 1990, 1991; V. V. Dwarkadas 2005). The structure of the surrounding medium may be further complicated by multiple episodes of eruptive mass loss (V. V. Dwarkadas 2007; D. J. Patnaude et al. 2015) leading up to the explosion. The SNRs of such events will evolve differently than explosions into a homogeneous medium with relatively fainter emission while the shock is propagating in the low-density medium followed by relatively brighter emission after the shock interacts with the denser material at the edge of the cavity. The evolution of the SNR depends on the details of the interior of the cavity and the shell that defines it (G. Tenorio-Tagle et al. 1990; V. V. Dwarkadas 2005). A strong stellar wind may create a low-density cavity with a radius of ∼15 pc (V. V. Dwarkadas 2007; Y. Chen et al. 2013) devoid of dense cores of molecular material while a weaker stellar wind might produce a smaller cavity or no cavity at all in which the dense cores from the MC complex survive passage of the forward shock of the SNR (R. A. Chevalier 1999). The observed characteristics of an SNR will differ dramatically depending on the structure of the medium that surrounded the star at the time of explosion, which in turn depends on the stellar wind and mass-loss history of the progenitor. Therefore, observations of SNRs in their current state provide important constraints on the type of star that exploded and how that star shaped its environment over its lifetime.

The Large Magellanic Cloud (LMC) SNR N132D is the most luminous SNR in X-rays in the Local Group with an X-ray luminosity of $L_X(0.3\text{–}10.0\,\mathrm{keV}) \sim 1 \times 10^{38}$ erg s^{-1}; only the SNR in NGC 4449 is more luminous in X-rays (D. J. Patnaude & R. A. Fesen 2003). It was first classified as a CCSN by B. E. Westerlund & D. S. Mathewson (1966), and has been subsequently studied in detail over the last few decades (F. Favata et al. 1997; X. Xiao & Y. Chen 2008; A. Bamba et al. 2018). Based on optical observations, it has been classified as an oxygen-rich remnant (I. J. Danziger & M. Dennefeld 1976; B. M. Lasker 1978, 1980), thought to have exploded inside a low-density cavity in the ISM. R. S. Sutherland & M. A. Dopita (1995) discuss the origin of this cavity, which might have formed due to a wind bubble mechanism common to Wolf–Rayet stars (V. V. Dwarkadas 2007). J. P. Hughes (1987) analyzed the X-ray data from the Einstein Observatory to conclude that a cavity explosion model could provide reasonable values of the explosion energy and age. It has been proposed by W. P. Blair et al. (2000) that this remnant might be the outcome of a Type Ib CCSN and is believed to be roughly 2500 yr old (J. A. Morse et al. 1995; J. P. Hughes et al. 1998; Y. Chen et al. 2003; F. Vogt & M. A. Dopita 2011). C. J. Law et al. (2020) performed a 3D reconstruction of the optically emitting O ejecta to refine the age estimate to 2450 ± 195 yr and J. Banovetz et al. (2023) derived a consistent age of 2770 ± 500 yr from proper-motion measurements of the O-rich ejecta based on multiepoch observations with the Hubble Space Telescope (HST).

Chandra X-ray Observatory (Chandra) observations (K. J. Borkowski et al. 2007) reveal a well-structured rim running along the southern part of the remnant. This well-defined rim is associated with dense MCs in this direction (K. R. Banas et al. 1997; H. Sano et al. 2015; H. Sano et al. 2020) and is also present in the infrared (IR) observations of dust continuum emission in N132D taken by Spitzer (B. J. Williams et al. 2006). N132D is a luminous GeV and TeV gamma-ray source (M. Ackermann et al. 2016; H. E. S. S. Collaboration et al. 2021; J. Vink et al. 2022b) with a location and spectrum that would be consistent with a hadronic origin due to interaction with the MC complex. The X-ray emission also shows a bright arc-shaped structure close to the outermost shell in the south and southeast that may be attributed to the reverse shock encountering the ejecta or face-on filaments produced by the forward shock interacting with density enhancements in the surrounding medium. P. Sharda et al. (2020) presented maps based on the Chandra data in narrow energy bands centered on the prominent K shell emission lines of O, Ne, Mg, Si, S, and Fe that showed the Fe K emission is distributed throughout the southern half of the remnant with a particularly bright region close to, but interior to, the southeastern shell. High-resolution spectra from the X-ray calorimeter on XRISM (XRISM Collaboration et al. 2024) show that the Fe Heα emission is broader than the Si and S emission and the Fe Lyα emission has a significantly higher redshift than the local ISM in the LMC, both consistent with an ejecta origin for the Fe K emission. XMM-Newton (XMM) observations (A. R. Foster et al. 2025) demonstrate that a plasma with a temperature of ∼4.5 keV is required to explain the Fe K emission and confirm the distribution of the Fe K emission in the southern half of the remnant.

H. Sano et al. (2020) detect evidence of shocked and clumpy CO material in the southern region and also toward the center of the remnant with the Atacama Large Millimeter/submillimeter Array. Toward the north, there are filament-like structures protruding outward that are relatively faint in X-rays compared to the rest of the remnant. The overall shape of the remnant resembles an ellipse, but the northern regions deviate from an elliptical shape with a fragmented and even box-like morphology in one region. The northern regions are significantly farther from the center of expansion (COE) as estimated by C. J. Law et al. (2020) and J. Banovetz et al. (2023), consistent with a higher average expansion velocity for these regions over the lifetime of the remnant. This morphology is consistent with an SNR shock encountering a roughly constant but higher-density medium in the south and a lower-density medium in the north.

Motivated by this morphology and the suggestion that N132D was produced by an SN in a preexisting cavity, Y. Chen et al. (2003) modeled the evolution of an SNR shock across a density jump, in which the medium before the jump has a lower density to represent the cavity and the medium after the jump has a higher density to represent the material swept up by the stellar wind. They applied their semianalytic model to N132D and found solutions that are consistent with an explosion energy of

$\epsilon_o \sim 3.0 \times 10^{51}$ erg, a preshock density of $n_o \sim 3.0\,\mathrm{cm}^{-3}$, an age of ~3000 yr, and a shock velocity of $v_s \sim 1.9 \times 10^3$ km s^{-1} before the shock encounters the cavity wall. They suggested that the forward shock may have decelerated to a velocity of $\sim 8.0 \times 10^2$ km s^{-1} after encountering the cavity wall in order to match the analysis of the X-ray data discussed in J. A. Morse et al. (1996). P. Sharda et al. (2020) used the high angular resolution Chandra data to extract spectra from narrow regions near the shock front to determine an average temperature of $kT = 0.85 \pm 0.20$ keV, which corresponds to a shock velocity of $v_s \sim 8.6 \times 10^2$ km s^{-1} assuming full equilibration between electrons and ions. They also estimated a progenitor mass of $15 \pm 5\,M_\odot$ based on the size of the cavity (Y. Chen et al. 2013) and the abundance ratios of ejecta-rich regions. A. R. Foster et al. (2025) estimate a progenitor mass of 13–15 $M_\odot$ based on the Ca/Fe and Ni/Fe ratios for the ejecta component in the XMM data.

The determination of the forward shock velocity, v_s, from X-ray spectral fits alone is subject to various difficulties that result in discrepancies with other methods, as described by J. C. Raymond et al. (2023). Among these difficulties are the fact that the extraction regions typically used for the X-ray spectral analysis are larger than the forward shock region, thereby including plasmas with different conditions, an unknown level of electron–ion equilibration, moderate- or low-resolution spectra, and inadequacy of the spectral models. J. Shimoda et al. (2015) point out that shocks propagating into an inhomogeneous medium will be rippled or oblique leading to an underestimate of the v_s based on the X-ray temperature alone. Given these challenges, any estimate of the forward shock velocity from X-ray spectral fits alone must be interpreted with these caveats in mind. Although the size of the cavity in N132D is well constrained by the existing Chandra data, the v_s is still uncertain.

A more direct method of determining the shock velocity is to measure the proper motion of a feature or features associated with the shock front, if the distance to the object is known or assumed. The high angular resolution of Chandra has been exploited to measure the proper motion of features in SNR shocks and to measure the global expansion of SNRs by comparing observations of the same remnant at different epochs. Chandra has measured the expansion rate at various locations in the youngest Galactic SNR G1.9+0.3 (K. J. Borkowski et al. 2017) to vary from 0.″09 yr^{-1} to 0.″44 yr^{-1}, which correspond to velocities of 3600 km s^{-1} to 17,000 km s^{-1} assuming a distance of 8.5 kpc. J. Vink et al. (2022a) have used Chandra to measure the proper motion of the forward shock (0.15–0.28% yr^{-1}, v_s = 4000–7000 km s^{-1}) and the reverse shock (−0.10–0.23% yr^{-1}, v_s = –1900–4200 km s^{-1}) at different locations in Cassiopeia A assuming a distance of 3.4 kpc. Chandra data have even been used to measure the expansion of SNRs in the Magellanic Clouds, which is considerably more difficult given the larger distance. L. Xi et al. (2019) measured an expansion of 0.025% yr^{-1} or a v_s of 1600 km s^{-1} for 1E 0102.2-7219 in the Small Magellanic Cloud assuming a distance of 60.6 kpc and B. J. Williams et al. (2018) measure velocities ranging from 2860 to 5450 km s^{-1} in the LMC SNR 0509-68.7 (N103B) assuming a distance of 50 kpc. These measurements are not subject to the systematic uncertainties of estimating the shock velocity from the fitted X-ray temperature, but have their own systematic uncertainties.

In this paper, we use new X-ray observations of N132D obtained as part of a Chandra Large Project (LP) to measure the proper motion of the forward shock and hence the v_s in the south and northeast, thereby circumventing the difficulties in determining the shock velocity based on spectral fits. These values are then used in 1D SNR evolution models to refine estimates of the explosion energy, ejecta mass, and ambient medium density and structure. The paper is organized as follows: Section 2 discusses the data, the initial reduction, and our registration method, Section 3 describes our expansion analysis and the estimate of the shock velocity, v_s. Section 4 presents the spectral analysis of narrow regions near the shock front. Sections 5 and 6 present the results of the 1D SNR models, the constraints on the explosion energy, ejecta mass, and ambient medium properties, and a comparison of the plasma temperature inferred from the X-ray spectral fits to the temperature inferred from the measured shock velocities, and finally in Section 7 we present our conclusions. The three appendices (Appendices A, B, and C) include more information on the details of the analysis. We assume the distance to N132D to be 50 kpc in all calculations hereafter (G. Clementini et al. 2003; G. Pietrzyński et al. 2013, 2019). At this distance, 1″ = 0.24 pc. All uncertainties reported are 1σ uncertainties unless noted otherwise.

2. Data and Reduction

2.1. Chandra Large Project

N132D was observed by Chandra for a total of 878 ks from 2019 March 27 to 2020 July 16 in 28 separate observations as part of a Chandra LP (proposal number 20500554, PI: Plucinsky); see Table 1 for details. The goals of the LP include studying the late stages of massive star evolution, the SN explosion mechanism, SN elemental abundances, ejecta properties and distribution, and the physical mechanisms for the interaction of shocks with MCs and cavities. This is the first paper in a series of papers from this Chandra legacy data set and focuses on the expansion of the forward shock and the evolution of the SNR. The data acquired in 2019–2020 (labeled as Epoch *B* in Table 1) are compared to the previous Chandra observations executed in 2006 (labeled as Epoch *A*), to measure the proper motion of different features in the remnant over an ~14.5 yr interval. A significant challenge for this analysis is the reduction in the low-energy sensitivity of the Advanced CCD Imaging Spectrometer (ACIS) instrument from 2006 to 2020 due to the accumulation of a contamination layer on the optical blocking filter (OBF; P. P. Plucinsky et al. 2016; P. P. Plucinsky et al. 2022). The analysis presented in this paper is restricted to the energy range of 1.2–7.0 keV unless otherwise stated to minimize the effect of the contamination correction on the results. Another challenge to this analysis is the fact that the 2019–2020 observations were executed in 28 distinct epochs. Not all of these observations are suitable for the expansion analysis described in this paper as explained later but may be used for future analyses. We describe in detail in the following sections our efforts to register these observations to take full advantage of Chandra's exquisite angular resolution.

2.2. Data Processing

We reprocessed each observation (see Table 1) generating new level 2 event lists using CIAO 4.13 (A. Fruscione et al. 2006) and CALDB 4.9.5, including the CIAO tool `chandra_repro`.[19]

[19] https://cxc.harvard.edu/ciao/ahelp/chandra_repro.html

Table 1
Observations List

ObsID	Start Date (YYYY-MM-DD)	Exposure (ks)	Roll Angle (deg)	Used to Measure Expansion?
Epoch *A*: 2006 January				
5532	2006-01-09	44.6	330.16	Y
7259	2006-01-10	24.8	330.16	Y
7266	2006-01-15	19.9	330.16	Y
Epoch *B*: 2019 March−2020 July				
21362	2019-03-27	34.4	255.62	Y[a]
21363	2019-08-29	46.0	105.15	Y[a]
21364	2019-09-01	20.8	105.15	⋯
22687	2019-09-02	34.4	102.66	Y[a]
22094	2019-09-10	36.2	93.15	Y[a]
21687	2019-09-11	24.7	93.15	⋯
22841	2019-09-12	36.5	93.15	Y[a]
22853	2019-09-22	19.8	83.30	⋯
22740	2019-09-26	19.8	78.15	⋯
22858	2019-09-27	19.8	78.15	⋯
22859	2019-09-28	18.8	78.15	⋯
21881	2019-10-04	23.3	60.15	⋯
22860	2019-10-06	17.8	60.15	⋯
23270	2020-05-29	27.7	178.14	⋯
21882	2020-05-30	34.6	178.14	Y[a]
21883	2020-05-31	32.6	178.14	Y[a]
23044	2020-06-02	52.9	175.15	Y[a]
21886	2020-06-05	43.0	175.14	Y[a]
21365	2020-06-07	56.3	175.14	Y[a]
23277	2020-06-08	14.9	183.13	⋯
21884	2020-06-09	42.5	183.14	Y[a]
21887	2020-06-10	51.4	183.14	Y[a]
21885	2020-06-25	21.3	167.15	⋯
23286	2020-06-27	14.9	167.14	⋯
21888	2020-07-11	24.7	152.15	⋯
23303	2020-07-12	24.7	152.14	⋯
21361	2020-07-13	31.1	160.14	Y[a]
23317	2020-07-16	43.1	160.14	Y[a]

Note.
[a] The observations used in the spectral analysis.

The default `pix_adj = EDSER` was applied. Spectra were extracted for the point sources, forward shock, and background regions, and the corresponding response files were created using `specextract` and analyzed in `Xspec` version 12.11.0k. The `FTOOLS` command `fkeyprint` was used to set the `AREASCAL` of the background spectra to the ratio of the source and background `BACKSCAL` to scale the background area to the source area. SAOTrace 2.0.5 and MARX 5.5.1 were used for simulating point-spread functions (PSFs) of the point sources (see Section 2.3.1 below for details.) To correct the for the quantum efficiency (QE) changing from the first 2006 observation to later observations, we use the CIAO tool `eff2evt` to get the QE for every event in each observation, by setting the option `detsubsysmod` to the start time of the corresponding observation. The added columns were renamed, and `eff2evt` was rerun with `detsubsysmod` set to the start time of the reference observation `ObsID` 23317. The CIAO tool `dmtcalc` was used to evaluate the event QE correction corresponding to the time of the reference observation. To merge the events lists of the 2006 observations and the 2019–2020 observations, we used the CIAO tool `reproject_events` to project each event list to the tangent point of the observation `ObsID` 5532, then we used `dmmerge` to merge the event lists. Figure 1 displays the merged image from the 2019–2020 data in the 1.2–7.0 keV band with the regions used for the expansion analysis indicated.

2.3. Registration of the Observations

We first obtain a list of common sources in the vicinity of the remnant (see Section 2.3.1 below) for each observation, and reposition the pointing to minimize the scatter in these point-source positions (see Section 2.3.2 below). Epoch *A* observations are each first individually registered to `ObsID` 5532, and Epoch *B* observations to `ObsID` 23317. The merged Epoch *A* data set is then matched to Epoch *B* by reregistering them to `ObsID` 23317.

2.3.1. Point-source Positions

To produce a list of point sources around the remnant for registration purposes, we run `wavdetect` (P. E. Freeman et al. 2002) on each observation. We select point-like sources that are detected in at least two observations, since sources detected in only one observation cannot be used in the registration of multiple observations. This results in a total of 50 point sources. For each pair of observations, we select point sources which are present in both observations. Of the 50 total sources detected, the number of common point sources for pairs of observations ranged from 10 to 22.

The off-axis angles of the detected sources range from $0.'9$ to $8'$. The position reported by `wavdetect` is not accurate enough for our purposes because the tool assumes a symmetric PSF. The PSF varies with off-axis angle, roll, and (to a lesser extent) energy. To obtain more accurate positions for point sources, we use SAOTrace[20] to model the X-ray optics and MARX[21] to model the detector and simulate a PSF image for each point source for each observation.

Though we select sources that appear to be point-like, we allow them to be extended by convolving the simulated PSF image with a Gaussian kernel. This practice is also in keeping with the suggested CIAO thread,[22] which also accounts for aspect uncertainty, residual systematics in the PSF model, as well as in superresolved binning (unless otherwise stated, we adopt a bin size of one-quarter of a sky pixel $\equiv 0''.123$).

SAOTrace can model a point source at the location of the source identified by `wavdetect` and MARX can apply the detector pixelization and detector response. Using these tools, we construct ray-traced point sources at the locations of the point-like sources, with $\approx 5000\times$ the estimated counts in order to minimize simulation fluctuations. These result in well-sampled images to construct the PSF model for fitting.

In Sherpa, we define a source model using a 2D symmetric Gaussian function plus a constant. The source model is convolved with the PSF image to make a "model image" for fitting the "data image." The data image is a point-source image extracted from the observation using a $31''.488 \times 31''.488$ box region. The data image and model image are both binned to $0''.0615 \times 0''.0615$ pixels. The center, amplitude, and sigma of the Gaussian function, and the

[20] https://cxc.cfa.harvard.edu/cal/Hrma/SAOTrace.html
[21] https://space.mit.edu/cxc/marx/
[22] https://cxc.cfa.harvard.edu/sherpa/threads/2dpsf/index.html#src

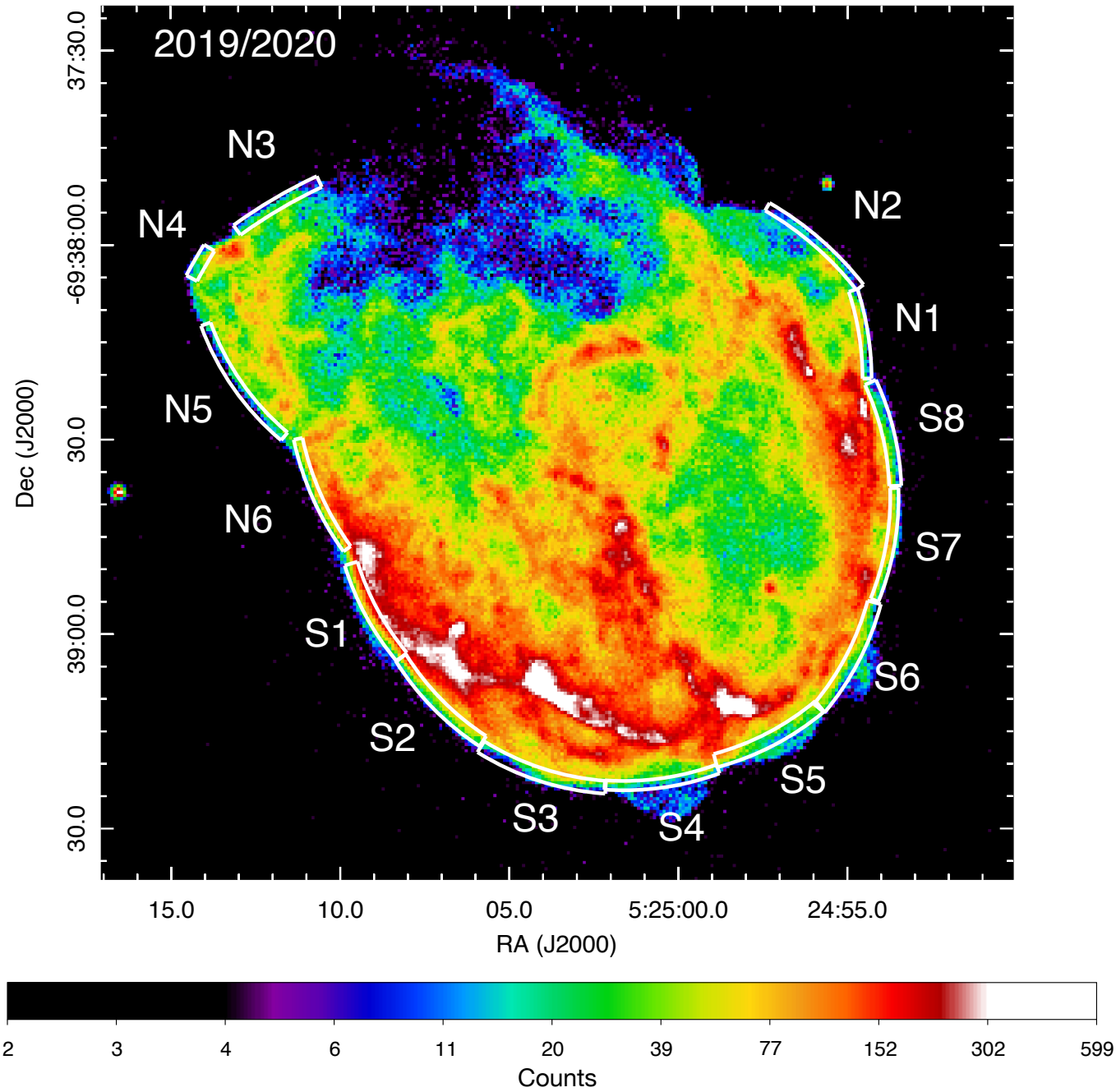

Figure 1. Chandra ACIS-S image of N132D in the energy band 1.2–7.0 keV produced from the LP data (Epoch *B*). The white arc regions (labeled S1–S8 along the southern rim and N1–N6 along the northern boundary) indicate the regions used for the expansion measurement and the spectral analysis. The bin size of the image is 0.″492. The units of the color bar are counts.

constant value are free to change. We use the C-statistic (C-stat; W. Cash 1979) as the fit statistic. The constant value accounts for the detector background level; it is reasonable to assume a constant background within the area of the point-source image. The position of the point source is taken to be the fitted center (x, y) of the Gaussian function. The 1σ errors of the position, (σ_x, σ_y), are calculated by varying the the x- or y-center positions along a grid of values while the values of the remaining free parameters are allowed to float to new best-fit values.

The accuracy and precision of this method is limited by the point-source counts and the off-axis angle. To characterize this, we simulate point sources with off-axis angles from 1′ to 6′ , and point-source counts from 5 to 400 counts. We apply the same PSF fitting method described above to obtain the positions and the position errors, and exclude sources within each observation which are outside the 5% and 95% quantiles of the distribution of distances from the best-fit power law of the distribution (see Appendix A for details).

We also exclude point sources which are located on or near the CCD boundary in an observation; although these point sources have enough counts to yield reasonable fitted positions, the positions may be biased toward the parts of the dithered image fully on the CCD. Nine point sources common to all of the observations remain after excluding the outliers. These are shown in Figure 2, and the coordinates of the point sources are

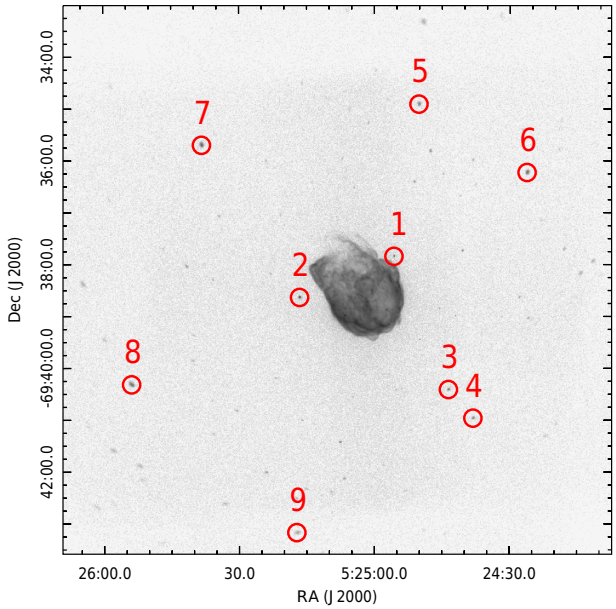

Figure 2. Point sources used in the registration are shown as labeled red circles on a merged Epoch *B* image. The circle labels are the point-source IDs (see Table 2). The image is binned to two ACIS sky pixels (0.″964), and the energy band is 1.2–7.0 keV; the image is shown in logarithmic gray scale.

listed in Table 2. For each pair of observations, the sources used for registration are listed in Table 3.

2.3.2. Registration Method

We register an observation to a reference observation by shifting the (x, y) positions of point sources in the observation to match the positions of the corresponding point sources in the reference observation. The shifted positions (x', y') for the observation to be matched are

$$\begin{pmatrix} x' \\ y' \end{pmatrix} = \begin{pmatrix} a_{11} & a_{12} \\ a_{21} & a_{22} \end{pmatrix} \begin{pmatrix} x \\ y \end{pmatrix} + \begin{pmatrix} t_1 \\ t_2 \end{pmatrix}, \quad (1)$$

where the parameters a_{11}, a_{12}, a_{21}, and a_{22} account for the scale factor and rotation, and t_1 and t_2 account for the x- and y-translations.

The position shifts are used to compute a transformation which minimizes the discrepancies. We use a loss function, D, that is robust to outliers; it trends to quadratic for small deviations, but approaches the magnitude of the differences for large deviations:[23]

$$D = \sum_{i=1}^{n} \left(\sqrt{1 + \frac{(x_i' - x_{0,i})^2}{\sigma_{x_i}^2 + \sigma_{x_{0,i}}^2} + \frac{(y_i' - y_{0,i})^2}{\sigma_{y_i}^2 + \sigma_{y_{0,i}}^2}} - 1 \right), \quad (2)$$

where n is the number of matched point sources, (x_i, y_i) is the position of source i, and $(x_{0,i}, y_{0,i})$ is the position of the corresponding reference source. The position error of source i is $(\sigma_{x,i}, \sigma_{y,i})$ and $(\sigma_{x_{0,i}}, \sigma_{y_{0,i}})$ is the position error of the corresponding reference source. Hereafter, the subscript i will be implicit and not shown unless necessary for disambiguation.

We used the CIAO tool `wcs_update` with the fitted parameters a_{11}, a_{12}, a_{21}, a_{22}, t_1, and t_2 to update the aspect solution file and the world coordinate system of the observation event list.

The error on the registration is estimated by the registration residual. The weighted average position residual for the matched point sources of the two observations is

$$r = \sqrt{(r_x)^2 + (r_y)^2} = \sqrt{\left(\frac{\sum^n \frac{(x' - x_0)}{\sigma_d^2}}{\sum^n \frac{1}{\sigma_d^2}} \right)^2 + \left(\frac{\sum^n \frac{(y' - y_0)}{\sigma_d^2}}{\sum^n \frac{1}{\sigma_d^2}} \right)^2}. \quad (3)$$

In Equation (3), r_x and r_y are the weighted average position residuals of the matched point sources in the x- and y-directions. The combined position error for each source is

$$\sigma_d = \sqrt{\sigma_{x'}^2 + \sigma_{x_0}^2 + \sigma_{y'}^2 + \sigma_{y_0}^2}. \quad (4)$$

We registered the Epoch *A* observations to `ObsID` 5532, and the Epoch *B* observations to `ObsID` 23317. We separately merged the Epoch *A* observations and the Epoch *B* observations to allow for an expansion measurement by comparing the epochs. The merged Epoch *A* observations are registered to the merged Epoch *B* observations using the point sources in common and the registration method described above. The resulting transformation matrix is applied to each of the Epoch *A* observations, and the Epoch *A* observations are remerged so that the merged Epoch *A* observations are registered to the merged Epoch *B* observations.

After registration, the positions and position errors of the point sources were obtained using the method described in Section 2.3.1. The registration results are shown in Table 3. The average registration residual of Epoch *A* observations is 1.0 mas ($\sim 2.4 \times 10^{-4}$ pc at the distance of the LMC), and the average registration residual of later observations is 5.6 mas. The average registration residual of the merged Epoch *A* observations and the merged Epoch *B* observations is 1.8 mas; we quote this value as the systematic error in the expansion measurement in Section 3. The errors of the registration residuals shown in Table 3 are the standard errors of the weighted average position residuals of the point sources used

Table 2
Sources Used in the Registration

Source ID	R.A. (J2000) (deg)	Decl. (J2000) (deg)
1	81.2319050	−69.6308336
2	81.3190858	−69.6440358
3	81.1814788	−69.6736206
4	81.1587763	−69.6828067
5	81.2089350	−69.5819136
6	81.1091962	−69.6038267
7	81.4094288	−69.5950900
8	81.4745292	−69.6720078
9	81.3218042	−69.7196139

[23] We use the `soft_l1` option of the SciPy (P. Virtanen et al. 2020) Python routine `scipy.optimize.least_squares`. This loss function is more robust than least squares or chi-squared since the weighting of outliers approaches a linear rather than quadratic penalty. In the limit $\{x, y\}_i' \to \{x, y\}_{0,i}$, $D \to \frac{1}{2}\left[\frac{(x_i' - x_{0,i})^2}{\sigma_{x_i}^2 + \sigma_{x_{0,i}}^2} + \frac{(y_i' - y_{0,i})^2}{\sigma_{y_i}^2 + \sigma_{y_{0,i}}^2} \right]$ while for large deviations, $D \to \sqrt{\frac{(x_i' - x_{0,i})^2}{\sigma_{x_i}^2 + \sigma_{x_{0,i}}^2} + \frac{(y_i' - y_{0,i})^2}{\sigma_{y_i}^2 + \sigma_{y_{0,i}}^2}}$.

Table 3
Registration Results for Each Observation

ObsID	ΔR.A. (arcsec)	ΔDecl. (arcsec)	Rotation Angle (deg)	Point-source IDs	Registration Residual $r_x \pm \sigma_{r_x}$ (mas)	$r_y \pm \sigma_{r_y}$ (mas)	$r \pm \sigma_r$ (mas)
(A) ObsIDs in Epoch 2006 registered to ObsID 5532							
7259	−0.0397	0.2776	0.0737	2, 3, 6, 8, 9	−0.9 ± 1.7	−0.7 ± 3.4	1.2 ± 3.8
7266	−0.0621	0.4177	−0.0066	2, 5, 6, 9	0.7 ± 2.2	−0.0 ± 0.1	0.7 ± 2.2
(B) ObsIDs in Epoch 2019–2020 registered to ObsID 23317							
21361	0.7020	−0.0945	0.0366	1, 2, 3, 5, 6, 7, 8	−8.0 ± 11.6	7.6 ± 7.4	11.0 ± 13.8
21362	1.3610	0.9308	−0.0060	1, 2, 3, 4, 6, 7	9.0 ± 17.3	3.8 ± 10.5	9.8 ± 20.2
21363	0.6201	0.3249	0.0559	1, 2, 3, 4, 6, 8	3.7 ± 6.2	0.0 ± 2.3	3.7 ± 6.6
21365	0.0916	0.2840	0.0031	1, 2, 3, 6, 7, 8	−0.8 ± 3.4	−0.6 ± 4.1	1.0 ± 5.4
21882	0.0214	0.3023	−0.0040	1, 2, 3, 5, 6, 7, 8	−2.7 ± 7.2	1.8 ± 2.3	3.3 ± 7.5
21883	0.0344	0.2665	0.0261	1, 2, 3, 5, 6, 7, 8	−1.0 ± 3.0	14.4 ± 9.2	14.4 ± 9.7
21884	−0.0178	0.2759	0.0108	1, 2, 4, 5, 6, 7, 8	2.9 ± 5.0	−0.3 ± 2.3	3.0 ± 5.5
21886	−0.0398	0.2609	−0.0088	1, 2, 3, 5, 6, 7, 8	−4.9 ± 4.9	3.1 ± 8.1	5.8 ± 9.4
21887	0.2173	0.2703	−0.0122	1, 2, 5, 6, 7, 8	−4.9 ± 5.9	3.7 ± 5.6	6.1 ± 8.2
22094	0.5311	−0.1047	−0.0085	1, 2, 3, 4, 6, 7	1.4 ± 3.6	0.6 ± 12.0	1.6 ± 12.6
22687	0.7102	0.1936	0.0588	1, 2, 3, 4, 5, 6	2.7 ± 5.1	−2.4 ± 4.4	3.6 ± 6.7
22841	0.8491	0.1365	0.0149	1, 2, 3, 4, 5, 6, 7	6.4 ± 11.8	−2.0 ± 9.5	6.7 ± 15.1
23044	0.2329	0.3599	0.0148	1, 2, 3, 5, 6, 7, 8	0.7 ± 6.1	2.8 ± 3.8	2.9 ± 7.2
(C) Combined Epoch 2006 (Epoch *A*) registered to the combined Epoch 2019–2020 (Epoch *B*)							
Epoch 2006	0.9039	0.5799	−0.0038	2, 3, 4, 5, 6, 8, 9	−0.9 ± 2.9	1.5 ± 1.3	1.8 ± 3.2

in the registration:

$$\sigma_r = \sqrt{(\sigma_{r_x})^2 + (\sigma_{r_y})^2} = \sqrt{\left(\frac{\sum^n \frac{(x' - x_0 - r_x)}{\sigma_d^2}}{\sqrt{n}\sum^n \frac{1}{\sigma_d^2}}\right)^2 + \left(\frac{\sum^n \frac{(y' - y_0 - r_y)}{\sigma_d^2}}{\sqrt{n}\sum^n \frac{1}{\sigma_d^2}}\right)^2}. \quad (5)$$

Here, σ_{r_x} and σ_{r_y} are the standard error of the average position residual of matched point sources in the x- and y-directions, separately.

In Figure 3 we show the cumulative counts distribution (1.2–7.0 keV) for (registered) point source number 2 (see Figure 2), for the merged Epoch *A* observations (in red) and the merged Epoch *B* observations (in blue). The cumulative distributions of the point sources from Epoch *A* and Epoch *B* observations are consistent with each other within a radius of 1.5 sky pixels (0.″738), and this range contains ∼70% of the enclosed counts, covering the core of the PSF. This indicates that the observations are well registered. The PSF difference between Epoch *A* and Epoch *B* can result in a possible systematic error in the measurement of expansion of 0.″026. We discuss this possible effect in Section 3.1.

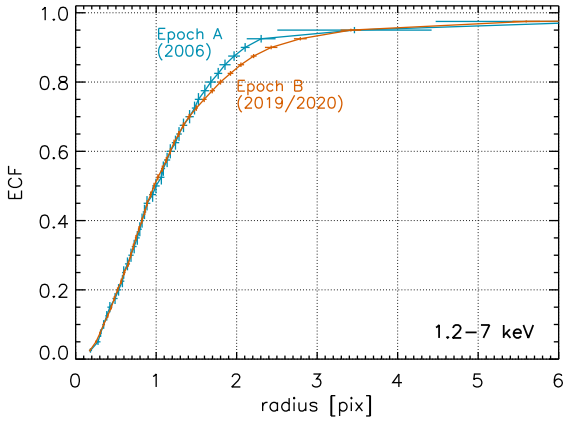

Figure 3. The cumulative radial enclosed counts fraction (ECF) in the two epochs for point source 2 (from Figure 2) in energy band 1.2–7.0 keV. The x-axis is the radius in ACIS "sky" pixels ("physical coordinates"). The narrower (blue) distribution, showing error bars at ECF intervals of 0.025, are for the merged Epoch *A* observations after registration. The broader (red) line and error bars are for the merged Epoch *B* observations after registration.

3. Expansion Analysis

We extract 1D radial profiles from the merged Epoch *A* and merged Epoch *B* event lists for 14 regions of interest around the edge of the remnant (shown in Figure 1). The regions are chosen to approximately follow the curvature of the edge of the remnant and have approximately similar angular extents, except for the N4 region. The southern regions are labeled S1 to S8 and the northern regions are labeled N1 to N6. The dimensions of the regions are determined based on the local counts profile along axes radiating outward from near the center of the remnant. First we identify peaks in the profile within ≈10″ of the edge and place the inner radius where the Epoch *A* counts profile falls to 80% of the peak. We then place the outer radius of the regions within the range where the counts profile is the steepest, excluding any protrusions visible in the broadband image. The dimensions and locations of the regions are listed in Table 4.

Because the QE of ACIS changes with time, we include a correction to the counts profiles so that shifts in the profile due to QE changes are not misinterpreted as expansion shifts. We do this by assigning each event a weight factor to correct the QE to a reference time, $t_{\rm ref}$, taken to be the start time of ObsID 23044:

$$t_{\rm ref} \equiv t\,[\text{start of ObsID 23044}]. \quad (6)$$

Table 4
Radial Profile Extraction Regions[a]

Region	Center R.A. (J2000) (deg)	Center Decl. (J2000) (deg)	Start Angle (deg)	Stop Angle (deg)	Inner Radius (arcsec)	Outer Radius (arcsec)
S1	81.2588809	−69.6436519	197	220	40.″132	42.″177
S2	81.2559342	−69.6448819	212	237	40.″784	42.″660
S3	81.2566376	−69.6449958	238	266	40.″804	42.″791
S4	81.2567163	−69.6447111	266	290	41.″748	43.″187
S5	81.2540938	−69.6442025	285	310	40.″812	42.″928
S6	81.2586843	−69.6455994	320	345	41.″484	43.″593
S7	81.2571130	−69.6441644	338	362	41.″584	42.″871
S8	81.2561512	−69.6440629	2	25	40.″242	42.″103
N1	81.2619398	−69.6390685	0	18	43.″476	44.″672
N2	81.2588729	−69.6436505	38	60	48.″968	50.″337
N3	81.2682702	−69.6499883	115	126	75.″976	77.″819
N4	81.2552309	−69.6448917	148	152	76.″714	78.″897
N5	81.2775545	−69.6328541	200	230	40.″012	41.″400
N6	81.2619398	−69.6390685	192	216	43.″984	45.″362

Note.
[a] A CIAO `dmregion` may be constructed for each extraction region of interest as `pie` (R.A., decl., inner radius, outer radius, start angle, and stop angle).

The weights are calculated from the QE at the start time of the observation and at $t_{\rm ref}$. For the Epoch A observations (2006), the weights are $w_{t_{A[i]}} = q(t_{A[i]})/q(t_{\rm ref})$, where $i = 1, 2, 3$ are the Epoch A `ObsID` indices: $t_{A[1]}$: `ObsID` 5532, $t_{A[2]}$: `ObsID` 7259, and $t_{A[3]}$: `ObsID` 7266), and $t_{A[i]}$ is the start time of the ith Epoch A observation. For the Epoch B observations (2019–2020) the weights are $w_{t_{B[j]}} = q(t_{B[j]})/q(t_{\rm ref})$, with Epoch B `ObsID` indices $j = 1, 2, 3, ..., 14$ (see Table 12 in Appendix B), and $t_{B[j]}$ is the start time of the jth Epoch B observation. Here, $q(t_{A[i]})$, $q(t_{B[j]})$, and $q(t_{\rm ref})$ are the QE values of the events, appropriate for the energy of the event obtained using the CIAO tool `eff2evt` where the option `detsub-sysmod` is set to the indicated time.

Because the total exposure times of the Epoch A and Epoch B observations are different, after the radial profiles are extracted, we scale the radial profiles from Epoch A to correct for the exposure time difference by using the scaling factor $s(t_A) = \tau_B/\tau_A$, where τ_A and τ_B are the respective total exposure times of the Epoch A and Epoch B observations,.

After the QE is corrected for the variation with time and the differences in exposure times are accounted for, we find the radial profiles from Epoch A and Epoch B for a given region, which can differ by ∼3%–7% because of residual QE differences between nodes (quadrants of the CCD, see Table 12 in Appendix B). These small, residual QE differences may be due to errors in the contamination model and/or the charge transfer inefficiency correction model for ACIS. The Epoch A observations have almost the same roll angle (330°), but the Epoch B observations have roll angles ranging from 80° to 256°. The events for a given region can be on different nodes of the S3 CCD depending on the roll. In our analysis, we have three combinations of epochs and node IDs for the events in a given region: (1) Epoch B events on node 1 and Epoch A events on node 0, (2) Epoch B events on node 0 and Epoch A events on node 0, and (3) Epoch B events on node 0 and Epoch A events on node 1.

To correct the QE difference to the same level event by event, we multiply the weights discussed before with a QE difference normalization according to the node ID and time epoch. The QE difference normalizations are$\mathcal{Q}(B1; A0)$ for Epoch B events on node 1 and Epoch A events on node 0, $\mathcal{Q}(B0; A0)$ for Epoch B events on node 0 and Epoch A events on node 0, and $\mathcal{Q}(B0; A1)$ for Epoch B events on node 0 and Epoch A events on node 1. The QE differences are corrected to the QE on node 0 at Epoch B. The QE difference normalizations are determined using the method discussed in Appendix B.

To measure the shift of the radial profile between the two epochs, we shift the events in the merged Epoch A data set in the radial direction, extract a radial profile in a prespecified radial region, and compare it against the corresponding radial profile obtained for the merged events of Epoch B. As discussed above, the QE change, exposure time differences, and QE difference normalizations are applied while extracting the radial profiles. We show the radial profiles of region S1 for illustration in Figure 4. All the regions used in this work are shown in Figure 1 and listed in Table 5. We calculate the C-stat between the Epoch A radial profile considered as the "model" and the Epoch B radial profile considered as the "data." This results in an array of C-stat values computed as a function of shifts of the Epoch A radial profile. Because this curve is affected by statistical fluctuations, we obtain a smooth representation by fitting it with a quadratic function around the minimum C-stat value. The shift corresponding to the minimum of the quadratic function is our estimate of the shifts between the Epoch A and Epoch B radial profiles. We select four data points to the left and right of the minimum C-stat value to include in the quadratic fitting. Figure 5 shows an example of such a fit for region 1. The 1σ error range is determined from the quadratic fit function by finding the range of shifts satisfying $y - y_m \leqslant 1$, where y is the quadratic function and y_m is the minimum value.

3.1. Expansion of the Forward Shock

We first consider the shifts for each region determined by the method described in the previous section and then consider the systematic errors and possible corrections to those errors. The expansion results and their uncertainties for the 14 regions indicated in Figure 1 are shown in Table 5 in the column labeled "raw shifts" and plotted in Figure 6. The expansion results are plotted as a function of the "region orientation angle," which we define as the angle between the normal

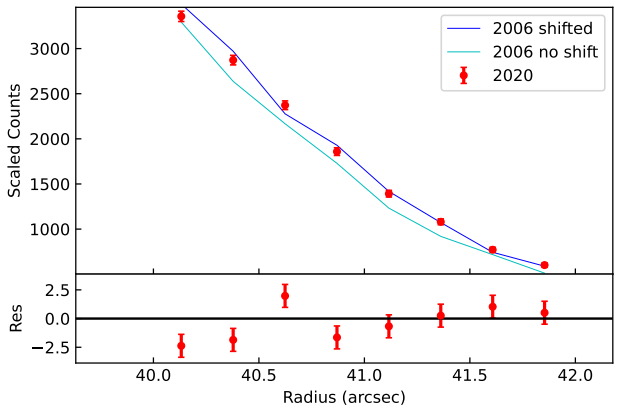

Figure 4. The radial profiles of region S1. The red data points are the profile of the 2019–2020 observations. The cyan line is the profile of the 2006 observations without a shift. The blue line is the 2006 profile shifted by the measured expansion. The lower panel shows the residuals of the 2020 profile and the shifted 2006 profile.

vector to the long dimension of the region and north in Figure 1. For most regions (such as regions S1–S8), this angle is close in value to that of the azimuthal angle with respect to north; but for some regions such as N3 and N5 it can be significantly different. We adopted this representation to more easily distinguish regions for which the normal vector does not point back to the supposed COE. The eight southern regions (S1–S8) lie on an approximately circular rim and are located at similar radii from the nominal COE (J. Banovetz et al. 2023). It would be reasonable to examine the case in which each of these eight regions had the same or similar expansion and compute an average expansion. Such a case yields an average expansion rate of $0\farcs11 \pm 0\farcs02$, or equivalently $1850 \pm 390\,\mathrm{km\ s^{-1}}$, for these regions.[24] The estimate and associated uncertainties are listed in Table 6 and are marked in Figure 6. A blue horizontal line spans the S1–S8 regions indicating the best fit for the average expansion. Note that seven of the eight regions are consistent with the average at the 1.5σ level, with region S4 being the sole outlier at $\approx 3\sigma$. This indicates that the assumed scenario of a common COE yielding the same expansion rate is a reasonable fit to the data for regions S1–S8, and perhaps also for the northern regions N1 and N5. However, the observed scatter could be an indication of inhomogeneous expansion. Note that regions N2, N3, and N4 are located at larger distances from the nominal center (see Table 5 for the distances from the centers of the regions to the expansion center) and have significantly larger expansion rates. The larger expansion velocities for N2, N3, and N4 are consistent with free (homologous) expansion ($v_s \propto R_s$) for those regions. The spatial velocities for regions N1, N6, and particularly N5 are less certain because their normals deviate significantly from the direction to the COE. Our method measures the velocities perpendicular to the region sectors; the parallel component is not determined. Thus, the actual velocities for N1, N6, and N5 could be larger than we assess.

We examined several potential systematic errors that could affect our result. One possible source of systematic error is due to the fact that the shape of the Chandra PSF is a function of the off-axis and azimuthal angles. Since our analysis includes data from the same region of the remnant acquired at different off-axis and azimuthal angles, it is possible that different shapes of the PSF could introduce a systematic error if the two data sets to be compared were acquired with different off-axis and azimuthal angles. Based on simulations of the PSF for the Epoch *A* and Epoch *B* observations, the differences in the PSF between epochs could mimic a (small) expansion or contraction. To measure this PSF bias effect, we simulated the merged PSF for each region and epoch as described in Appendix C. The differences show an azimuthal variation which we fit with a sinusoid. To correct for this PSF bias, we subtracted the fitted sinusoidal model from the expansion results in Figure 6 to obtain a PSF-bias-corrected expansion as shown in Figure 20 in Appendix C. The amplitude of this effect can be as large as ∼40 mas.

We also consider a systematic error in the effective expansion center we assumed for the southern rim. We initially assume that the southern regions are expanding uniformly. Any bias in the effective expansion center would tend to increase or decrease the measured expansion in directions 180° opposite to each other, resulting in a sinusoidal variation with azimuth. We fit the measured expansion of the southern regions (corrected for PSF bias) with a sinusoidal function as described in Appendix C shown in the blue curve in Figure 21. This fit indicated that the COE should be shifted by $0\farcs05$ in R.A. and $0\farcs02$ in decl. if the eight southern regions are assumed to have a uniform expansion. We subtract this sinusoidal variation to obtain the final expansion results listed as the "corrected shifts" in Table 5 and shown in Figure 7.

The comparison between Figures 6 and 7 shows that the combined effect of these two corrections is small and the average expansion for the eight southern regions only changes by ∼13% after the corrections are applied. The average expansion of the eight southern regions is $0\farcs10 \pm 0\farcs02$ after applying both corrections (see "corrected" shift in Table 6), giving an average expansion velocity of $1620 \pm 400\,\mathrm{km\,s^{-1}}$. The relation of the expansion of the southern regions to the average expansion is similar to the "raw shifts" results in that seven of the eight regions are consistent with a constant expansion rate at the 2σ level, with region S4 being the sole outlier at 2.5σ. Regions N1 and N5 are also consistent with the average expansion rate while region N2 is more than 3σ higher and N6 is 3σ lower. The lower expansion for the N6 region might be due to the fact that our method is only sensitive to the velocity component that is in the same direction as the normal to the long axis of the region or a possible impedance by the molecular material seen in the ^{12}CO maps of H. Sano et al. (2017). The northeastern regions N3 and N4 have similar expansion values and given their proximity, we combine them to get an average expansion for the northeast rim. The average raw expansion for regions N3 and N4 is $0\farcs22 \pm 0\farcs02$ corresponding to a velocity of $3630 \pm 260\,\mathrm{km\,s^{-1}}$ (see Table 6) and the corrected average expansion is $0\farcs23 \pm 0\farcs02$, with an average expansion velocity of $3840 \pm 260\,\mathrm{km\,s^{-1}}$,

[24] We compute the average expansion for the $M = 8$ southern regions and estimate the error on the average by combining the individual statistical errors (the so-called within variance, *W*) and the possible systematic errors based on the observed scatter in the estimates (the between variance, *B*). We use the method described in H. Lee et al. (2011, see their Equations (5)–(7)) to compute the total variance):

$$T = W + \frac{M+1}{M}B,$$

for a sample size of *M*. Note that this is a conservative estimate of the error bars on the expansion, and assumes the existence of systematic biases, which manifest in the scatter of the expansion estimates for the different regions.

Table 5
Expansion Measurements of the Regions S1–S8 and N1–N6

Region	Orientation[a]	Distance[b]	Raw[c]		Corrected[d]	
			Shift	Velocity	Shift	Velocity
	(deg)	(arcsec)	(arcsec)	(km s^{-1})	(arcsec)	(km s^{-1})
S1	118.5	41.99	0.″098 ± 0.″009	1640 ± 160	0.″090 ± 0.″009	1510 ± 160
S2	134.5	41.36	0.″127 ± 0.″014	2130 ± 230	0.″115 ± 0.″014	1920 ± 230
S3	162.0	42.53	0.″104 ± 0.″011	1740 ± 180	0.″085 ± 0.″011	1420 ± 180
S4	188.0	42.19	0.″145 ± 0.″011	2420 ± 180	0.″122 ± 0.″011	2050 ± 180
S5	207.5	41.64	0.″086 ± 0.″017	1450 ± 290	0.″064 ± 0.″017	1080 ± 290
S6	242.5	41.78	0.″113 ± 0.″010	1900 ± 170	0.″097 ± 0.″010	1630 ± 170
S7	260.0	41.29	0.″095 ± 0.″014	1590 ± 240	0.″083 ± 0.″014	1390 ± 240
S8	283.5	42.42	0.″109 ± 0.″011	1820 ± 180	0.″105 ± 0.″011	1760 ± 180
N1	279.0	45.98	0.″112 ± 0.″012	1880 ± 190	0.″107 ± 0.″012	1790 ± 190
N2	319.0	51.11	0.″146 ± 0.″012	2440 ± 200	0.″153 ± 0.″012	2560 ± 200
N3	30.5	71.64	0.″212 ± 0.″029	3560 ± 480	0.″228 ± 0.″029	3810 ± 480
N4	60.0	76.11	0.″221 ± 0.″012	3700 ± 210	0.″231 ± 0.″012	3870 ± 210
N5	125.0	62.71	0.″117 ± 0.″008	1970 ± 130	0.″108 ± 0.″008	1810 ± 130
N6	114.0	47.53	0.″074 ± 0.″009	1240 ± 150	0.″068 ± 0.″009	1140 ± 150

Notes.
[a] The counterclockwise angle of the direction of the normal vector of the regions from north, as in Figure 8.
[b] The distance of region centers to the COE in Table 7.
[c] Raw estimates of expansion, prior to correction for PSF bias and expansion center shift.
[d] PSF bias and effective expansion center bias corrected result.

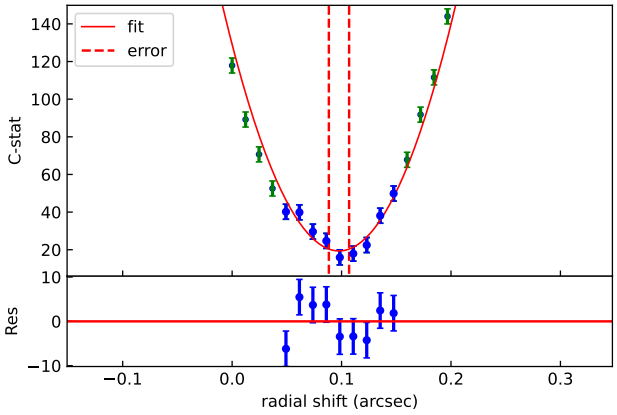

Figure 5. The C-stat variation with position shift for region S1. The green and blue data points are the C-stat calculated from the 2020 profile and shifted 2006 profile at the shift positions. The blue data points are included in the quadratic fitting for the shift estimate. The red solid line is the fitted quadratic function. The vertical dashed lines show the 1σ error range of the estimated shifts.

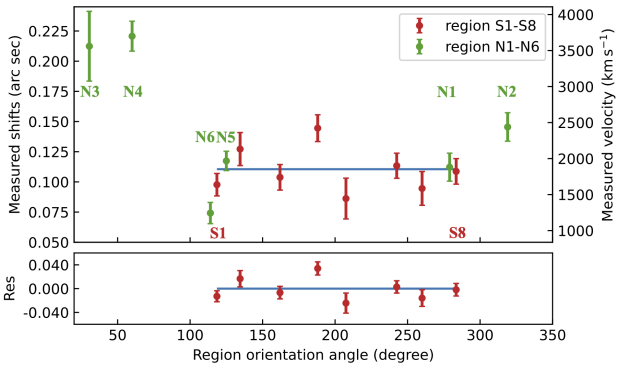

Figure 6. The raw measured expansion of the S1–S8 (labeled sequentially from left to right) and N1–N6 regions ("raw shifts" in Table 5), with the fitted average expansion (blue solid line) from the S1–S8 regions.

clearly much larger than the average expansion rate of the eight southern regions. Regions N3 and N4 also have the largest radii with respect to the COE, consistent with their larger expansion values. It is worth noting that our estimate of the COE shown in Figure 8 and listed in Table 7 assumed a symmetric explosion for the S1–S8 regions, while the COE analysis of J. Banovetz et al. (2023) did not. Our COE estimate differs by 1.″5 or 0.4 pc from the J. Banovetz et al. (2023) COE; both of which differ from the J. A. Morse et al. (1995) estimate by 9.″2 or 2.2 pc. The picture that emerges from this expansion analysis is that regions S1–S8 have a similar expansion history and similar current expansion rate while some of the N1–N6 regions have significantly different expansions histories and/or current expansion rates.

4. Spectral Analysis

We extracted spectra from the regions used for the expansion analysis as indicated in Figure 1. These narrow regions near the outer extent of the remnant should be dominated by emission from the ISM swept up by the forward shock and should have little or no contribution from ejecta emission. We used the set of 14 observations (summed exposure time of 574.8 ks) from Epoch *B* that were registered to each other for the expansion analysis to ensure that the spectra were extracted from as close to the same region as possible. Off-remnant background spectra were extracted for each observation individually given the different roll angles of the observations and point sources were excluded in these background regions. Spectral files and the necessary response files for spectral fitting were generated with the CIAO tool `specextract`.

We fit the source spectrum in `Xspec` version 12.11.0k (K. A. Arnaud 1996) with a `vpshock` model (K. J. Borkowski et al. 2001) appropriate for a plane-parallel shock with a constant temperature. The `wilms` (J. Wilms et al. 2000) abundances and the `vern` (D. A. Verner & D. G. Yakovlev 1995) photoelectric cross sections are used. We used a

Table 6
Average Expansion for the Southern Rim and Northeast Rim: Raw and Corrected Estimates

Measurement	Average Expansion (Velocity)	Within Error[a]	Between Error[a]	Total Error	χ^2 (DOF)
Southern (raw)	0.″111 (1850 km s^{-1})	0.″012	0.″019	0.″023	16.60 (7)
Southern (corrected)	0.″097 (1620 km s^{-1})	0.″013	0.″019	0.″024	12.80 (5)
N3 + N4 (raw)	0.″217 (3630 km s^{-1})	...	...	0.″016	...
N3 + N4 (corrected)	0.″230 (3840 km s^{-1})	...	...	0.″016	...

Notes. The degrees of freedom (DOF) are shown in the final column.
[a] The scatter of measurements within and the mean estimated uncertainties, see footnote 24.

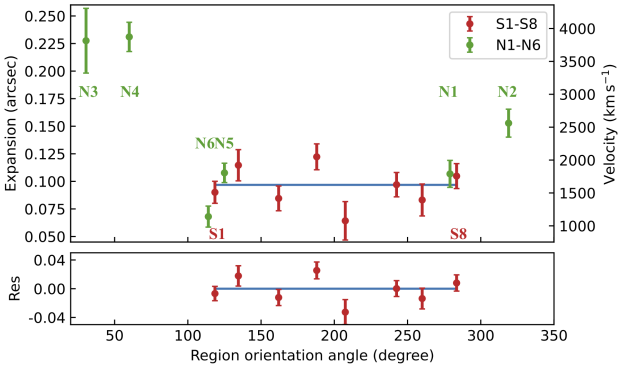

Figure 7. As in Figure 6, but for the final expansion estimates. The expansion of each region ("corrected shifts" in Table 5) is based on the raw shifts shown in Figure 6, corrected for the PSF bias and COE bias. The blue solid line shows the average expansion of the S1–S8 regions.

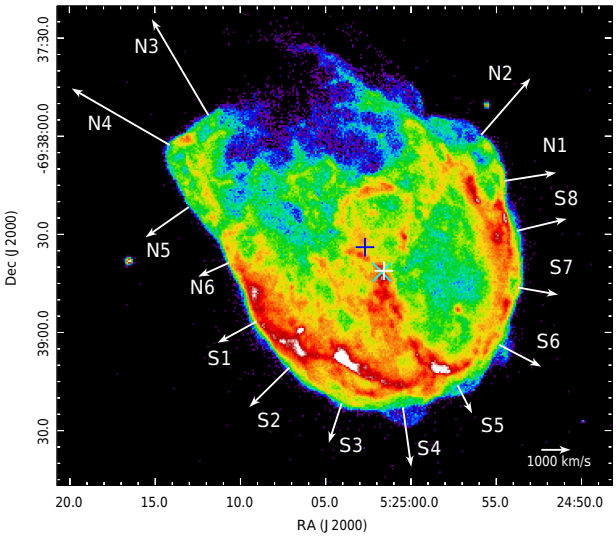

Figure 8. The expansion of N132D along selected regions around the rim. The arrows point in the direction of the orientation of the regions (see Table 5), and their lengths are proportional to the estimated expansion velocities. The COE (white cross) is estimated assuming that the regions along the southern rim (S1–S8) lie on a circular rim, and their orientations closely follow the azimuthal locations of the rim (for comparison, the COE of the optical knots is also shown as the cyan cross; J. Banovetz et al. 2023; and the blue plus J. A. Morse et al. 1995). The orientations of the regions along the northern rim (N1–N6) are substantially different from their azimuthal locations relative to the COE.

two-component absorption model, with one component (tbabs) for the Galactic line-of-sight absorption, fixed at $N_{\rm H,Galactic} = 0.047 \times 10^{22}$ cm^{-2} (HI4PI Collaboration et al. 2016), and another (tbvarabs) for the LMC absorption, $N_{\rm H,LMC}$, with the elemental abundances set to 0.5 × solar abundances. A background model was constructed consisting of detector and sky background components and fit to the background spectra simultaneously with the source spectra. The detector background model was based on the ACIS instrumental background described in H. Suzuki et al. (2021). The sky background model includes two thermal components for the foreground emission from the Galaxy and the LMC and also a component resulting from N132D produced as the CCD is being read out (the so-called "transfer streak"). We also included a nonthermal component for the extragalactic background. The data were unbinned for the fitting process and have only been binned for display purposes. The C-stat was used as the fit statistic to determine the best-fitted values of the parameters.

Table 7
Center of Expansion Estimates

Expansion Center	R.A. (J2000)	Decl. (J2000)
J. A. Morse et al. (1995)	$05^{\rm h}25^{\rm m}02\overset{\rm s}{.}70$	−69°38′34.″00
J. Banovetz et al. (2023)	$05^{\rm h}25^{\rm m}01\overset{\rm s}{.}71$	−69°38′41.″64
This work[a]	$05^{\rm h}25^{\rm m}01\overset{\rm s}{.}59$	−69°38′41.″20

Note.
[a] Estimated expansion center based on regions S1–S8.

A representative spectrum from region S2 from the Epoch *B* data is displayed in Figure 9 with the source and summed background models overplotted. This figure shows that the source flux dominates the background in the 0.5–5.0 keV band given the brightness of N132D. Therefore most of the parameters of the source model are relatively insensitive to the background model. The ACIS effective area has changed significantly between 2006 and 2019–2020 owing to the buildup of a contamination layer on the OBF in front of the CCDs (P. P. Plucinsky et al. 2016). At the energy of the bright O VIII Lyα line at 0.654 keV, the effective area decreased by about a factor of 4 between the two epochs. We therefore decided to fix the O abundance and $N_{\rm H,LMC}$ for Epoch *B* as follows: we fit the Epoch *A* spectrum for each region with a vpshock model allowing the $N_{\rm H,LMC}$, the O, Ne, Mg, Si, S, and Fe abundances, the ionization timescale, the temperature, and the normalization to vary in order to obtain the $N_{\rm H,LMC}$ and O abundance for each region. We then fit the Epoch *B* spectrum for each region using a vpshock model with the O abundance and the $N_{\rm H,LMC}$ fixed at the Epoch *A* values. The vpshock abundances for Ne, Mg, Si, S, and Fe, the ionization timescale, the temperature, and the normalization were free to vary for the Epoch *B* spectral fits. As seen in Figure 9, the Epoch *B* spectra peak around 1.0 keV of the energy of the Ne lines. Therefore, useful constraints on the Ne, Mg, Si, S, and Fe abundances may be obtained from the Epoch

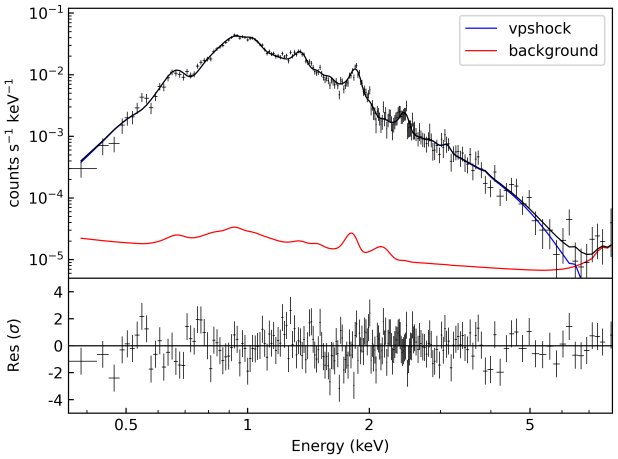

Figure 9. The spectrum of region S2 from the Epoch *B* data fit with a `vpshock` model and the background model. The black points and line are the spectral data and model. The red line is the background model. The `vpshock` model parameters are listed in Table 8.

B spectra given the ACIS effective area at the time of those observations and the relatively large summed exposure of the Epoch *B* observations.

The fit results for the regions are listed in Table 8. All of the fits are acceptable as determined by the value of the C-stat and the DOF. There is no reason to explore a more complicated spectral model as a single `vpshock` component is sufficient to represent these moderate-resolution ($E/\Delta E \sim 15$) spectra to the statistical precision afforded by the number of counts in the spectra. The fitted values of the $N_{\rm H,LMC}$ indicate that the absorbing column is higher in the southern regions than the northern regions, a pattern which was described in P. Sharda et al. (2020). The fitted values of the electron temperature range from 0.76 to 1.20 keV in the southern regions and from 0.72 to 0.94 keV in the northern regions. The highest temperatures are observed for regions S1–S4, while the lowest temperatures are observed for regions S6 and S7 and N3–N5. The fitted values of the ionization timescale range from a minimum value of 0.61×10^{11} cm^{-3} s for the N2 region to a maximum value of 2.23×10^{11} cm^{-3} s for the S7 region. Nevertheless, 10 of the 14 fits are clustered around an ionization timescale of $1.0 \pm 0.5 \times 10^{11}$ cm^{-3} s suggesting a similarity in the underlying spectra. The element abundances are consistent with the LMC ISM abundances ($\approx$0.5 $\times$ solar). This implies that these regions are free of a significant contribution from ejecta emission and are representative of the forward shock conditions. In general, these spectral fit results are in good agreement with those in P. Sharda et al. (2020), which were based on the Epoch *A* data alone. Given that the southern regions S1–S8 have a similar expansion with respect to each other and the regions N3 and N4 have a similar expansion with respect to each other, it is instructive to explore the average properties of these regions. The southern regions have an emission-measure-weighted average temperature and ionization timescale of 0.95 ± 0.17 keV and $1.39 \pm 0.49 \times 10^{11}$ cm^{-3} s respectively, where the uncertainties are the multiple-imputation total variances as described earlier. The regions N3 and N4 have an emission-measure-weighted average temperature and ionization timescale of 0.77 ± 0.04 keV and $1.28 \pm 0.17 \times 10^{11}$ cm^{-3} s respectively. One would naively expect the temperatures of the northern regions to be higher given that our measured shock velocities are higher in the north. In Section 5 we discuss the relation of the temperature estimates based on fits to the X-ray spectra to the temperatures implied by the shock expansion estimates, and consider possible explanations for the discrepancies.

5. Temperature Comparison from Expansion versus Spectral Model

In Section 3.1 we evaluated the velocities of the outer shocks based on proper-motion measurements for various regions on the rim: S1–S8 along the roughly circular rim in the south, and N1–N6 at various positions in the northeast and northwest. In Section 4, we extracted spectra for those same regions and evaluated the electron temperature based on the thermal plasma X-ray emission.

Because energy equilibration and ionization processes take time, the X-ray spectra give the electron temperature for conditions far from complete equilibration. In this section we discuss the degree to which the electron thermal pool has equilibrated, and whether the X-ray temperatures are consistent with the ion temperatures estimated from the proper-motion velocity.

For a steady, planar shock with velocity $v_{s,n}$ perpendicular to the shock interface, in an ideal gas with $\gamma = 5/3$ and particles of mass m, the Rankine–Hugoniot conditions imply a temperature

$$kT = \frac{3}{16} m v_{s,n}^2. \quad (7)$$

In an electron–ion plasma, the mass-proportional electron temperature $kT_{e,mp}$, proton temperature $kT_{p,mp}$, and average temperature kT_{av} are obtain by substituting m with m_e, m_p, and μm_p, respectively. Here, μ is the mean mass per free particle in units of the proton mass (1 amu). For a fully ionized plasma with "cosmic" abundances (J. Wilms et al. 2000), $\mu \approx 0.61$. The mass-proportional electron temperature is $T_{e,mp} = (m_e/m_p)T_{p,mp} \lll T_{e,mp}$, that is, the electrons start out cold (a few electron volts for typical SNR shock speeds). Some form of electron–ion equilibration is needed for there to be electron thermal temperatures of $\sim$1 keV. In a collisionless plasma, the equilibration between electron and ion temperatures proceeds via Coulomb interactions at least. This process is slow and the effective collisional mean free path can exceed the dimensions of the SNR. In such cases, collisionless equilibration in the shock may be needed to explain the excess of electron temperature over the Coulomb-equilibrated value.

In Section 3.1 we found the average proper-motion expansion velocity for the eight southern regions to be $v_{s,n} = 1620 \pm 400$ km s^{-1}, while for N3 and N4 in the northeast, the average expansion velocity is higher at $v_{s,n} = 3840 \pm 260$ km s^{-1}. In Table 9 we show the resulting mean temperature based on the proper motion, $kT_{pm,av}$, assuming a fully ionized plasma with $\mu = 0.61$, and the corresponding mass-proportional proton and electron temperatures, $kT_{p,mp}$ and $kT_{e,mp}$, respectively. The measured X-ray-based temperatures in Section 4 (see Table 8) are clearly far from full equilibration, but are also elevated above the mass-proportional electron temperatures $kT_{e,mp}$. Additional collisionless heating is not indicated since it would make the electron temperature discrepancy worse.

There must be at least Coulomb equilibration in the plasma, which increases T_e from the mass-proportional value

Table 8
Spectral Fit Parameters for the Epoch *B* Spectra with the 1σ Uncertainties Assuming a `vpshock` Model

Region	$N_{H_{LMC}}$ [a] (10^{22} cm^{-2})	kT_e (keV)	τ (10^{11} cm^{-3} s)	Norm (10^{-4})	O	Ne	Mg	Si	S	Fe	C-stat	DOF
S1	0.12	$0.98^{+0.02}_{-0.02}$	$1.48^{+0.10}_{-0.10}$	$6.16^{+0.24}_{-0.24}$	0.45	$0.52^{+0.03}_{-0.03}$	$0.36^{+0.02}_{-0.02}$	$0.49^{+0.03}_{-0.03}$	$0.52^{+0.06}_{-0.05}$	$0.37^{+0.02}_{-0.02}$	12,824	14,634
S2	0.07	$1.20^{+0.04}_{-0.04}$	$1.39^{+0.17}_{-0.12}$	$1.97^{+0.15}_{-0.11}$	0.66	$0.51^{+0.06}_{-0.06}$	$0.47^{+0.05}_{-0.05}$	$0.61^{+0.05}_{-0.06}$	$0.40^{+0.08}_{-0.07}$	$0.51^{+0.04}_{-0.04}$	12,174	14,634
S3	0.15	$1.14^{+0.05}_{-0.04}$	$0.88^{+0.09}_{-0.09}$	$1.44^{+0.09}_{-0.10}$	0.35	$0.40^{+0.06}_{-0.05}$	$0.45^{+0.05}_{-0.04}$	$0.55^{+0.06}_{-0.06}$	$0.59^{+0.12}_{-0.11}$	$0.51^{+0.06}_{-0.05}$	11,787	14,634
S4	0.17	$1.01^{+0.10}_{-0.07}$	$1.54^{+0.39}_{-0.33}$	$0.80^{+0.11}_{-0.11}$	0.60	$0.39^{+0.09}_{-0.08}$	$0.51^{+0.08}_{-0.07}$	$0.49^{+0.08}_{-0.08}$	$0.66^{+0.17}_{-0.15}$	$0.53^{+0.09}_{-0.08}$	11,397	14,634
S5	0.11	$0.94^{+0.04}_{-0.03}$	$1.36^{+0.11}_{-0.17}$	$2.12^{+0.11}_{-0.15}$	0.68	$0.45^{+0.05}_{-0.05}$	$0.52^{+0.05}_{-0.05}$	$0.61^{+0.06}_{-0.05}$	$0.72^{+0.12}_{-0.10}$	$0.62^{+0.06}_{-0.05}$	11,945	14,634
S6	0.17	$0.76^{+0.02}_{-0.01}$	$1.09^{+0.12}_{-0.09}$	$3.43^{+0.19}_{-0.20}$	0.38	$0.54^{+0.03}_{-0.02}$	$0.45^{+0.03}_{-0.03}$	$0.50^{+0.04}_{-0.05}$	$0.65^{+0.13}_{-0.10}$	$0.38^{+0.03}_{-0.02}$	11,777	14,634
S7	0.05	$0.79^{+0.02}_{-0.02}$	$2.23^{+0.20}_{-0.20}$	$2.04^{+0.19}_{-0.12}$	0.54	$0.64^{+0.05}_{-0.05}$	$0.63^{+0.04}_{-0.05}$	$0.62^{+0.06}_{-0.06}$	$0.47^{+0.10}_{-0.10}$	$0.49^{+0.02}_{-0.05}$	11,276	14,634
S8	0.07	$0.91^{+0.04}_{-0.03}$	$0.98^{+0.10}_{-0.12}$	$1.18^{+0.07}_{-0.09}$	0.48	$0.60^{+0.06}_{-0.06}$	$0.46^{+0.06}_{-0.05}$	$0.58^{+0.08}_{-0.07}$	$0.46^{+0.16}_{-0.12}$	$0.49^{+0.06}_{-0.02}$	11,221	14,634
N1	0.09	$0.81^{+0.05}_{-0.04}$	$1.14^{+0.19}_{-0.21}$	$1.20^{+0.11}_{-0.13}$	0.54	$0.64^{+0.06}_{-0.05}$	$0.49^{+0.06}_{-0.05}$	$0.57^{+0.08}_{-0.07}$	$0.64^{+0.18}_{-0.17}$	$0.40^{+0.05}_{-0.05}$	11,078	14,634
N2	0.02	$0.94^{+0.06}_{-0.05}$	$0.61^{+0.10}_{-0.09}$	$0.60^{+0.05}_{-0.05}$	0.43	$0.78^{+0.07}_{-0.06}$	$0.50^{+0.07}_{-0.06}$	$0.65^{+0.11}_{-0.10}$	$0.84^{+0.29}_{-0.25}$	$0.33^{+0.05}_{-0.05}$	10,853	14,634
N3	0.05	$0.77^{+0.05}_{-0.03}$	$1.37^{+0.24}_{-0.25}$	$1.25^{+0.11}_{-0.13}$	0.28	$0.40^{+0.04}_{-0.05}$	$0.28^{+0.05}_{-0.04}$	$0.44^{+0.08}_{-0.07}$	$0.50^{+0.18}_{-0.16}$	$0.35^{+0.05}_{-0.04}$	11,220	14,634
N4	0.04	$0.77^{+0.06}_{-0.04}$	$1.15^{+0.23}_{-0.21}$	$0.83^{+0.09}_{-0.10}$	0.32	$0.52^{+0.06}_{-0.05}$	$0.26^{+0.06}_{-0.05}$	$0.31^{+0.08}_{-0.07}$	$0.52^{+0.22}_{-0.20}$	$0.28^{+0.05}_{-0.04}$	10,661	14,634
N5	0.01	$0.72^{+0.03}_{-0.03}$	$1.03^{+0.12}_{-0.15}$	$1.14^{+0.09}_{-0.09}$	0.45	$0.67^{+0.05}_{-0.05}$	$0.46^{+0.06}_{-0.05}$	$0.53^{+0.09}_{-0.08}$	$1.31^{+0.30}_{-0.27}$	$0.49^{+0.05}_{-0.05}$	11,045	14,634
N6	0.04	$0.74^{+0.03}_{-0.02}$	$1.65^{+0.18}_{-0.18}$	$3.28^{+0.20}_{-0.21}$	0.40	$0.55^{+0.03}_{-0.04}$	$0.51^{+0.05}_{-0.04}$	$0.53^{+0.04}_{-0.04}$	$0.66^{+0.14}_{-0.12}$	$0.49^{+0.05}_{-0.02}$	11,609	14,634

Note.
[a] Parameter value fixed to the value determined from the spectral fit to the Epoch *A* spectra.

$T_{e0} = (m_e/m_p)T_{p0}$ and correspondingly reduces the proton temperatures T_p. Because the flows are expanding, adiabatic expansion will also slightly reduce T_e. In the following, we examine these effects.

The temperatures of the electrons and protons will equilibrate via Coulomb collisions. To estimate this equilibration, we assume a fully ionized H plasma, $n_e = n_p$. A pair of coupled differential equations determines the time evolution of the proton and electron temperatures:

$$\frac{dT_e}{d(n_e t)} = -\frac{dT_p}{d(n_e t)} = 0.13\left(\frac{T_p - T_e}{2T_e^{3/2}}\right), \quad (8)$$

(see J. M. Laming & U. Hwang 2003, their Equations (B7) and (B8) for $Z = 1$), where the densities are in units of cm^{-3}, t is in s, and T_p and T_e are in units of K. We compute the plasma temperature in thin shells behind the shock and integrate Equation (8) from $n_e t = 0$ at the shock to 1.39×10^{11} cm^{-3} s at the innermost shell, with $\Delta(n_e\, t)$ constant for each shell. We solve the equations using Runge–Kutta integration `scipy.integrate.solve_ivp`, and compute the emission-measure-weighted temperatures across the width of the shock. Combined with the estimated shock velocity of $v_{pm} = 1620 \pm 400$ km s^{-1} for the southern rim, this yields an emission-measure-weighted electron temperature $kT_e = 0.89 \pm 0.43$ keV. The uncertainty is estimated by propagating the fractional uncertainty due to the uncertainty on the velocity estimate. A similar calculation for the northeastern regions, adopting a forward shock velocity of $v_{pm} = 3840 \pm 260$ km s^{-1}, and carrying out the integration over the range $n_e t = 0$ to 1.28×10^{11} cm^{-3} s^{-1}, yields an emission-measure-weighted electron temperature $kT_e = 1.84 \pm 0.23$ keV.

For adiabatic cooling, the integration limits for each shell are set by assuming homologous expansion from a common center (see Table 7), and that the radial distance determines the timescale for the cooling. Including the effects of adiabatic cooling reduces the temperature to $kT_e = 0.80 \pm 0.39$ keV for the southern rim and $kT_e = 1.74 \pm 0.22$ keV for the northeastern regions.

Table 9
Temperatures Derived from the Proper-motion Velocity (See Text)

Regions	$v_{s,n}$ (km s^{-1})	$kT_{pm,av}$ (keV)	$kT_{p,mp}$ (keV)	$kT_{e,mp}$ (keV)
S1–S8	1620 ± 400	$3.14^{+1.75}_{-1.36}$	$5.15^{+2.86}_{-2.23}$	$2.80^{+0.16}_{-0.12} \times 10^{-3}$
N3–N4	3840 ± 260	$17.6^{+2.5}_{-2.31}$	$28.0^{+4.1}_{-3.8}$	$1.57^{+0.22}_{-0.21} \times 10^{-3}$

In Table 10, we compare the electron temperature $kT_{e,ce+ad}$, based on the proper-motion velocity, v_{pm}, and corrected for Coulomb equilibration and adiabatic expansion, to the electron temperature, $kT_{e,x}$, based on the X-ray spectral fits. The $kT_{e,x}$ values are emission-weighted values for regions S1 to S8 and for N3 + N4. The temperature $kT_{e,ce+ad}$ for the southern rim is consistent with the temperature estimated from spectral fitting, but for the northeastern regions, $kT_{e,ce+ad}$ is significantly higher than $kT_{e,x}$.

We discuss some possible origins of this discrepancy in the next sections. In Section 5.1 we examine shock obliquity effects (see J. Shimoda et al. 2015). In Section 5.2, we examine the temperatures and shock velocities obtained by Y. Okada et al. (2025) for a set of N132D regions using the `IONTENP Xspec` table model developed by Y. Ohshiro et al. (2024), which provides a self-consistent 1D planar shock model. Finally, in Section 5.3, we consider possible energy losses due to cosmic-ray acceleration.

5.1. Rippled-shock Obliquities

As discussed in J. Shimoda et al. (2015), as an SNR blast wave propagates into a clumpy ISM the shock slows in the denser portions and moves faster in the lower-density portions between so that the shock refracts around the denser clumps. This results in a shock interface which is rippled, with locally oblique shocks. For an oblique shock, the velocity component parallel to the shock interface is conserved, so that the temperature jump depends only on the velocity component normal to the shock. If the angle between the flow velocity and the local shock normal is θ, the component normal to the shock

Table 10
Temperatures Based on Proper Motion vs. Corrected Temperatures

Regions	Velocity	Derived from Expansion Velocity[a]			Derived from X-Ray Fits		Ratio
	v_{pm} (km s^{-1})	$kT_{e,ce+ad}$ (keV)	$kT_{p,ce+ad}$ (keV)	$kT_{av,ce+ad}$ (keV)	$kT_{e,x}$ (keV)	$n_e\,t$ (cm^{-3} s)	$kT_{e,x}/(kT_{e,ce+ad})$
S1–S8	1620 ± 400	0.80 ± 0.39	3.90 ± 1.90	2.87 ± 0.62	0.95 ± 0.17	$(1.39 \pm 0.49) \times 10^{11}$	1.19 ± 0.62
N3–N4	3840 ± 260	1.74 ± 0.22	25.84 ± 3.27	16.82 ± 2.13	0.77 ± 0.04	$(1.28 \pm 0.17) \times 10^{11}$	0.42 ± 0.06

Note.
[a] "ce + ad:" after Coulomb equilibration and adiabatic expansion.

is $v_{s,n} = v_s \cos\theta$. The downstream temperature is proportional to $v_{s,n}^2$, so the immediate downstream temperature is reduced by a factor of $\cos^2\theta$:

$$kT_{ds} = kT_{pm} \cos^2\theta \leqslant kT_{pm}, \tag{9}$$

where kT_{pm} is the temperature obtained from the proper-motion velocity, and kT_{ds} is the temperature immediately downstream of a shock with angle θ. For a shock propagating through a clumpy medium, the postshock temperature is reduced by a factor of $\langle\cos^2\theta\rangle$, which is an average of the deflections within the region under consideration.

J. Shimoda et al. (2015) assume a mean interstellar gas density $\langle\rho\rangle_0$ with dispersion $\Delta\rho = (\langle\rho\rangle^2 - \langle\rho\rangle_0^2)^{1/2}$. To estimate the scales, they note that the turbulence in the ISM is likely driven by SNRs with an injection length scale $L_{\rm inj} \sim 100$ pc with density fluctuations at the injection scale of $\Delta\rho_{L_{\rm inj}} \sim 1$. In the turbulent medium these fluctuations cascade to smaller scales. They argue that the typical dispersion at scale λ is $\Delta\rho_\lambda/\langle\rho\rangle \simeq (\lambda/L_{\rm inj})^{1/3}$ and suggest that for $\lambda \sim 2$ pc, $\Delta\rho/\langle\rho\rangle_0 \sim 0.3$, a typical ISM value. To simplify the notation, we define $w \equiv \Delta\rho/\langle\rho\rangle_0$.

Direct measurements of the fluctuation scales in the neighborhood of N132D are not available. For the southern parts of N132D the tangential length scales are ∼3 pc for the faint protrusions beyond regions S4, S5, and S6 (see Figure 1), suggesting fluctuation scales of that length in the ambient medium. The scales for regions N3 and N4 are 3.5 pc and 1.2 pc, respectively. Using HST imaging followed up with Wide Field Spectrograph spectroscopy, M. A. Dopita et al. (2018) have identified a number of H I clouds of about 1 pc in size interacting with N132D (see their Figures 1 and 2, and our Figure 10 in which the clouds and our extraction regions are plotted on the HST Hα (F658N) image). Based on the above scales one might expect $w \sim 0.2$ or 0.3.

J. Shimoda et al. (2015) obtain an analytical estimate to constrain $\eta \equiv (T_{pm} - T_{ds})/T_{pm} = 1 - T_{ds}/T_{pm}$ based on w where T_{pm} and T_{ds} are the average temperatures of all particles:

$$w^2 \lesssim \eta \lesssim 2w. \tag{10}$$

We thus estimate

$$\begin{aligned} w = 0.2: &\quad 0.04 \lesssim \eta \lesssim 0.4, \\ w = 0.3: &\quad 0.09 \lesssim \eta \lesssim 0.6. \end{aligned} \tag{11}$$

For the N3 + N4 region in the northeast, the mean temperature based on the proper-motion velocity is $kT_{pm,av} = 17.6^{+2.5}_{-2.3}$ keV (see Table 9). If we take into account Coulomb equilibration and adiabatic expansion, the mean temperature based on the proper-motion velocity is reduced to 16.8 ± 2.1 keV, with the electron temperature becoming 1.74 ± 0.22 keV (see Table 10). This electron temperature still greatly exceeds the 0.77 ± 0.04 keV measured from the X-ray spectra.

To assess the degree to which shock obliquities could account for the difference, we estimate the initial mean temperature, $kT_{av,0} = 2.85$ keV, such that the mass-proportional electron temperature, $kT_{e0} = 2.5 \times 10^{-3}$ keV reaches the X-ray-based electron temperature after Coulomb equilibration and adiabatic expansion: $kT_{e0,ce+ad} \equiv kT_{e,x} = 0.77$ keV. Taking $kT_{av,0} = 2.85$ keV as kT_{ds} and comparing it to the temperature based on proper-motion velocity, $kT_{pm,av} = 17.6$ keV, implies $\eta = 0.84$, which is well beyond the ranges for shock obliquity effects given in Equation (11) for $w = 0.2$ or $w = 0.3$. Propagation into a clumpy medium and the resulting shock obliquities may explain part, but not all, of the discrepancies seen in the northeast.

Besides the likely shock obliquities due to propagation into a clumpy medium, N132D also shows larger-scale oblique shocks such as regions N6 and N5 in the northeast and N1 in the northwest, whose shock normals are at an angle to the direction to the expansion center. Note that our approach to measuring expansion necessarily provides the normal shock velocity $v_{s,n}$—it is insensitive to velocity components tangential to the shock surface. Thus, for these shocks, additional corrections for shock obliquity are not needed. An exception is the N4 region, which does not fully follow the shock surface. The edge of the remnant within the N4 region has obliquities on the sides of 20° to 30°, resulting in a temperature reduction of 12% to 25% based on Equation (9). Assuming that the region approximately divides into three azimuthal pieces with obliquities of 20°, 0°, and 30°, respectively, the net temperature reduction would be ∼12%, not enough to explain the temperature discrepancy.

Finally, the northeast is the site of an H I cloud–shock interaction (M. A. Dopita et al. 2018, cloud P01, see their Figures 2 and 3). In Figure 10, we plot the HST Hα image (F658N) with the M. A. Dopita et al. (2018) cloud positions plotted as yellow circles. We also plot Chandra X-ray contours (1.2–7.0 keV) and our extraction regions S1–S8 and N1–N6. The inset figure shows a blowup of the N3 and N4 region. The P01 cloud coincides with an X-ray enhancement, likely produced by the increased pressure in the reflected shock region. The overpressure drives a slower shock into the cloud, producing the optical emission (Hα emission, and [O III] emission as the cloud shock becomes radiative). The X-ray rim to the north also shows a slight concavity between region N3 and the eastern part of N4, indicative of oblique shocks generated as the shock refracts around the H I cloud. In selecting the N4 and N3 extraction regions, we attempted to avoid the cloud interaction, but it is possible that they still include some of the oblique shocks in the cloud interaction. If the cloud had a diffuse H I envelope, this would also decelerate

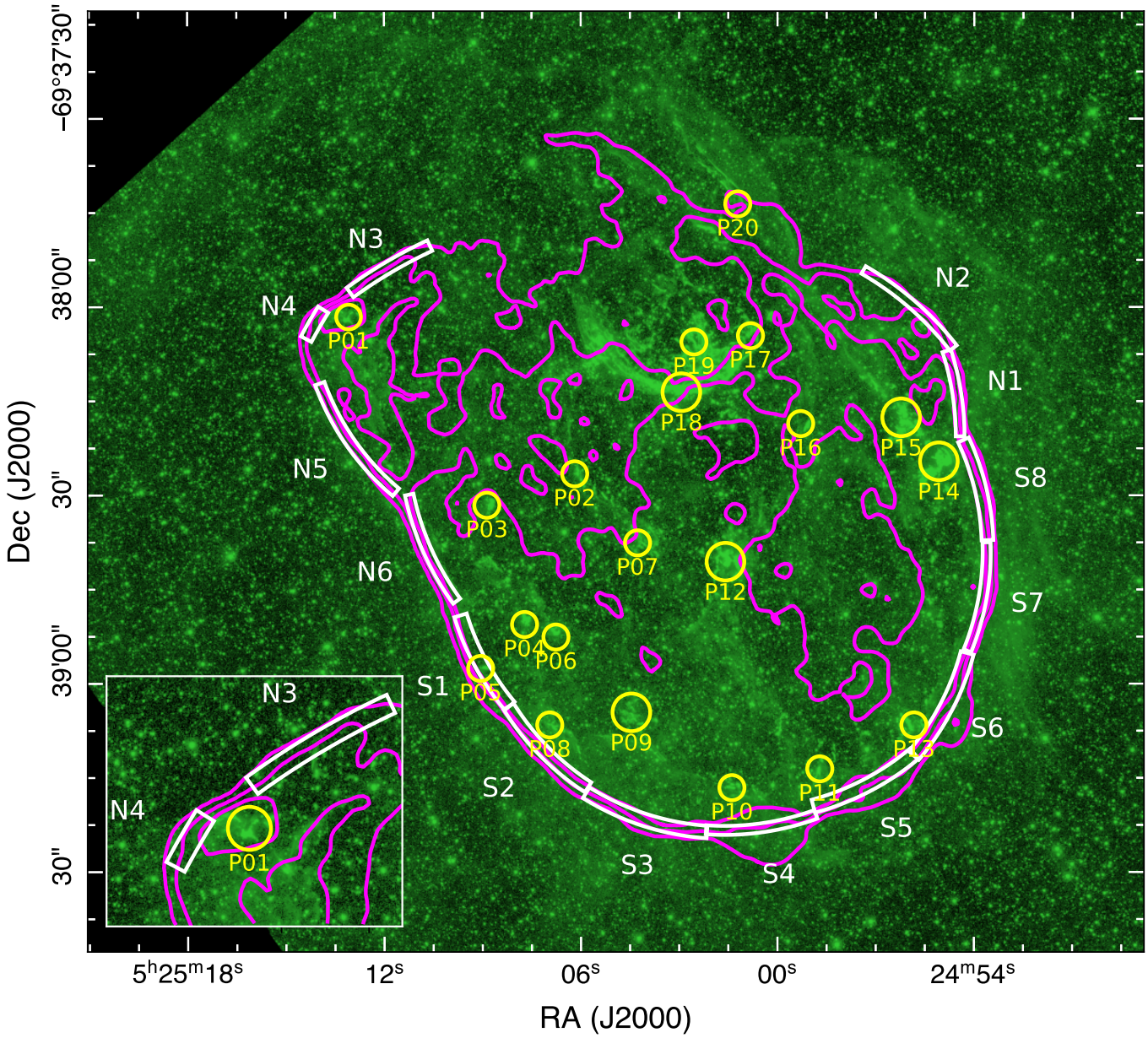

Figure 10. M. A. Dopita et al. (2018) shocked Hα-cloud regions displayed on the HST Hα (F658N) image with Chandra 2019–2020 (1.2–7.0 keV) contours in purple. Our expansion and spectral analysis regions are plotted in white. The inset shows an expanded view of the northeast. Cloud P01 shows indications of having interacted with the blast wave in the northeast—see the indentation in the X-ray contours in the inset and the X-ray enhancement in Figure 1. The small cloud P05 shows no indication of significant interaction in region S1.

the shock and might explain part of the lower temperatures obtained in the X-ray spectral fitting.

5.2. Shock Model Fits

Y. Ohshiro et al. (2024) have implemented an `Xspec` table model, `IONTENP`, for a self-consistent 1D shock model in which the changing electron density and temperature states are followed downstream of the shock, including the effects of Coulomb equilibration between ions and electrons. The shock velocity is a parameter in the fitting. This is in contrast to the `Xspec NEI` class of models (e.g., `VNEI` or `PSHOCK`) where the postshock electron temperature and the density are held constant. Y. Ohshiro et al. (2024) compared synthesized X-ray spectra (0.5–2 keV) for an `IONTENP` model with an `NEI` model with the same ionization timescale (10^{11} cm^{-3} s). The `IONTENP` model assumed a velocity of 1000 km s^{-1} and $kT_e/kT_{\rm ion} = 0.01$, where $kT_{\rm ion}$ is the mean ion temperature immediately behind the shock. The `NEI` model was used to synthesize a corresponding spectrum for $kT_e = 0.91$ keV, which is the temperature at 10^{11} cm^{-3} s in the `IONTENP` model. They find that n_et is about 30% smaller for `IONTENP` than for `NEI`, and the emission differs at lower energies since the plasma is cooler as energy is taken by the ionization processes.

Y. Ohshiro et al. (2024) examined a few regions of N132D and Y. Okada et al. (2025) conducted a more extensive analysis of the rim of N132D using merged Chandra LP data totaling 838 ks. Compared to the current work, the data were not spatially coaligned before merging, and the selection of

regions differ. In the present work, the regions are spatially narrower ($1\farcs3 - 2\farcs1$) extending past the shock surface in order to capture the edge of the shock structure, avoiding the brighter material interior to the shock. Y. Okada et al. (2025) use regions which are thicker ($3''$) and the regions appear to be somewhat inside the edge (see their Figure 1). In addition, there are partial azimuthal overlaps with our regions, and some of their regions (r16 and r17) do not overlap our regions at all. Our N4 region has no significant overlap with their region r1. Their regions r5–r10 approximately coincide with our S1–S5, and r11–r13 approximately coincide with S6–S7.

For r5–r10 versus S1–S5, the emission-weighted temperatures are consistent: $kT_e = 1.11 \pm 0.10$ keV and 1.03 ± 0.03 keV, respectively. For S6–S7 compared to r11–r13, our temperature is about 14% lower. For r2 + r3 versus S5, we are about 7% higher, but within the uncertainties.

For r1 (approximately overlapping our N4 region and extending into the gap between N4 and N3), the temperature agrees well with our N4 and N3 regions. They also compare $v_{\rm th,xray}$ with v_{pm} where the $v_{\rm th,xray}$ is the shock velocity estimated from spectral fitting, and v_{pm} is the proper-motion velocity. They find that region r1 is the most discrepant. However, this region has significant overlap with the M. A. Dopita et al. (2018) P01 H I shock–cloud interaction (see Section 5.1). The region includes multicomponent plasmas including the reflected shock from the cloud interaction and the oblique shocks as the blast wave refracts around the cloud. As noted in Section 5.1, a possible cloud envelope and the oblique refracted shocks may also result in cooler X-ray temperatures, which may be responsible for some of the r1 discrepancy. The reflected shock region (see Figure 10 inset) includes double-shocked material (blast wave, then reflected shock), which further compresses and heats the plasma. This double-shocked material and oblique shocks complicate the interpretation of the $v_{\rm th,xray}$ parameter of the `IONTENP` model; the reflected shock results in multiple temperatures from the two shocks (blast wave and shock reflection).

5.3. Cosmic-ray Acceleration

SNRs in the Galaxy younger than 2000 yr with shock speeds larger than 2500 km s^{-1} have been observed to produce detectable X-ray synchrotron emission (E. A. Helder et al. 2012). If this synchrotron emission is produced by efficient cosmic-ray acceleration by the shocks, it would remove energy from the shocks and reduce the shock temperature (A. Decourchelle et al. 2000; D. C. Ellison et al. 2007; D. J. Patnaude et al. 2009). We consider the possibility of electron synchrotron emission by adding a power-law component to the spectral model for region N4. We assume a power-law index of 3.0, and the resulting fit is shown in Figure 11. The C-stat (DOF) for the original model is 10,661 (14,634), and when the power-law component is added, we get C-stat (DOF) 10,655 (14,633). The power-law component does not significantly improve the fit and is not needed to explain the data. Given the power-law normalization, we can integrate the model flux over the energy band 0.35–8.0 keV, to obtain an upper limit on the power-law component flux of $1.68^{+0.21}_{-0.67} \times 10^{-14}$ erg s^{-1} cm^{-2}. This compares to a flux in the thermal component of $1.76^{+0.08}_{-0.08} \times 10^{-13}$ erg s^{-1} cm^{-2} in the 0.35–8.0 keV band. Therefore, the upper limit of any nonthermal contribution is less than 10% of the total flux. The intensity of the X-ray synchrotron emission depends on the density of electrons responsible for the emission and the strength and structure of the magnetic field (J. C. Houck & G. E. Allen 2006; G. E. Allen et al. 2008) in the emitting region. The density is in general low in the northeast part of N132D ($\sim$0.01 amu cm^{-3}, see Section 6.2) and our measured shock speed of 3620 km s^{-1} for the northeast should result in a cutoff frequency for the synchrotron emission around 0.5 keV (E. A. Helder et al. 2012). Therefore, it seems plausible that any X-ray synchrotron emission is too faint to be detected in this region. It is unlikely that cosmic-ray acceleration can explain the discrepancy in region N4 between $kT_{pm,ce+ad}$ and $T_{e,x}$.

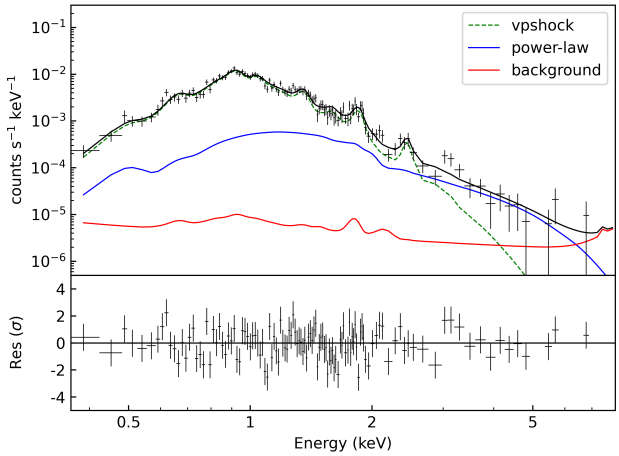

Figure 11. The spectrum of shock region N4 fit with a `vpshock` + power-law model and the background model. The black points and line are the spectral data and model, respectively. The green dashed line is the `vpshock` component. The blue line is the power-law component with an index of three. The red line is the background model.

6. Supernova Remnant Models

6.1. One-dimensional Shock Models

We generate analytic solutions following the work of J. K. Truelove & C. F. McKee (1999, hereafter TM99, 2000), as extended by J. M. Laming & U. Hwang (2003), U. Hwang & J. M. Laming (2012), and E. R. Micelotta et al. (2016). L. I. Sedov (1982) noted that the Euler equations do not contain any dimensioned constants, and that dimensional aspects are introduced through initial and boundary conditions. Here, the initial conditions introduce three dimensioned parameters: E (explosion energy in erg), $M_{\rm ej}$ (mass of the ejecta in solar masses), and ρ_0 (mass density of the preshock medium in units of g cm^{-3}). For the ejecta distribution, the core is taken to have constant density for simplicity, surrounded by an envelope described by a power-law distribution with index n. TM99 note that the distribution of mass and energy depends on n; for $n < 3$, mass and energy are concentrated in the outer (high-speed) ejecta, while for $n > 5$, mass and energy are concentrated in the inner (low-speed) ejecta. R. A. Chevalier & C. Fransson (1994) suggest indices $n \geqslant 7$ for CCSNe and lower indices for Type Ia SNe. Our explorations showed that the results were relatively insensitive to n for $n > 7$; in our treatment below we set $n = 9$ to be in the middle of the range of the values suggested by R. A. Chevalier & C. Fransson (1994).

The preshock ambient medium is also assumed to follow a power-law distribution:

$$\rho \propto \rho_0(r)/r^s, \tag{12}$$

where s is zero or two, and $\rho_0(r)$ is the ambient medium mass density just ahead of the shock. For the $s = 0$ case (constant density ambient medium) the value of $\rho_0(r)$ is constant. For the $s = 2$ case (ambient density falls as r^{-2}, appropriate for a constant stellar wind), the value of $\rho_0(r)$ pertains to a particular choice for the blast-wave radius, $R_{\rm b,0}$, so that $\rho(r) = \rho_0/(r/R_{\rm b,0})^2$. The introduction of a power-law ambient medium density distribution does not introduce additional dimensioned constants and the ejecta structure function is a dimensionless function, so asymptotic similarity solutions can still be constructed. Note that the r^{-2} ambient medium is assumed to be stationary ($v_{\rm wind} \equiv 0$). This implies that the velocity of the constant wind should be much smaller than the forward shock velocity. Incorporating a significant wind velocity would introduce an additional dimensioned parameter, significantly complicating the solution. These two assumed profiles for the ambient medium are simplifications of the true 3D structure, which is undoubtedly more complex due to variations in the stellar-wind properties over the life of the star and multidimensional effects that can produce hydrodynamical instabilities (V. V. Dwarkadas 2005, 2007). More sophisticated models use a lognormal (P. Padoan & Å. Nordlund 2011) or lognormal and power-law (B. Burkhart 2018) probability distribution function for the density of the medium. Nevertheless, the global properties of the bubble as predicted by 1D simulations should be similar to those from multidimensional simulations (V. V. Dwarkadas 2007) as the differences will manifest themselves on smaller spatial scales.

TM99 produced a detailed treatment of the $s = 0$ case, but only a limited treatment of the $s = 2$ case. U. Hwang & J. M. Laming (2003), J. M. Laming & U. Hwang (2003), and E. R. Micelotta et al. (2016) extend the treatment to a more detailed consideration of the $s = 2$ case. We refer the reader to these papers for the details. Here, we touch mainly on those aspects relevant to our analysis.

6.2. Remnant Evolution

We define the blast-wave radius as $R_{b,0}$ and the preshock density as $\rho(r)$ for the following discussion. For $s = 0$, $\rho(r) = \rho_0$ is constant, while for $s = 2$, $\rho(r) = \rho_0/(r/R_{b,0})^s$. For the $s = 2$ case we follow E. R. Micelotta et al. (2016), while for the $s = 0$ case, we follow TM99. The $s = 2$ (constant wind) case is an oversimplification of the evolution of the star before the explosion; however, it is useful to contrast this with the uniform medium case (itself a simplification since the ambient medium is likely to be inhomogeneous).

Our models depend on three dimensioned parameters, E, $M_{\rm ej}$, and ρ_0, plus two dimensionless structure parameters, n and s, for a total of five adjustable parameters. The ambient medium mass density is related to the hydrogen number density, n_0, by $n_0 = (\rho_0/\mu_{\rm H})/(1\ {\rm cm}^{-3})$ where $\mu_{\rm H}$ is the mean mass per hydrogen nucleus, assuming cosmic abundances. As noted in Section 6.1, the solutions are relatively insensitive to n for $n \geqslant 7$, and we adopt $n = 9$. We consider the $s = 0$ and $s = 2$ cases separately. For each s value, we consider ejecta masses of 2, 4, 6, and 8 $M_\odot$. We chose $E = 1.5 \times 10^{51}$ erg as the explosion energy for these initial calculations but explore different values later in this section. Our observational constraints are the measured blast-wave velocity, v_b, and the observed blast-wave radius, R_b. The ejecta mass, $M_{\rm ej}$, explosion energy, E, and structure parameters n and s are fixed, leaving a single free parameter, ρ_0, to be varied. We vary ρ_0 until the blast-wave radius and velocity, R_b and v_b, are matched.

Once the match is found, the remnant age can be evaluated based on the parameters of the model. For the southern rim and the $s = 0$ case, a circumstellar density of ρ_0 of $0.33^{+0.25}_{-0.12}$ amu cm^{-3} matches the observed v_b and R_b. The remnant ages of the $s = 0$ case are consistent with the age estimates from the optical observations (C. J. Law et al. 2020; J. Banovetz et al. 2023) as shown in Table 11. The calculated reverse shock radius ranges from $5.60^{+0.95}_{-2.33}$ pc to $7.27^{+0.07}_{-0.28}$ pc, for ejecta masses, $M_{\rm ej}$, from 2 to 8 $M_\odot$, respectively. From the X-ray morphology it appears that the reverse shock is relatively close in radius to the forward shock in the southern rim of the remnant. For the southern rim and the $s = 2$ case, a circumstellar density of ρ_0 of $0.22^{+0.17}_{-0.08}$ amu cm^{-3} matches the observed v_b and R_b. However, the estimated ages are ∼4200 yr, which are discrepant with the estimates from the optical at the 1.5σ level. In addition, the predicted location of the reverse shock is farther from the forward shock and closer to the center of the remnant with values ranging from $2.30^{+1.97}_{-2.30}$ pc to $5.98^{+0.16}_{-0.71}$ pc. The uniform ambient medium profile is more consistent with the estimated age from the optical and the apparent position of the reverse shock assuming this 1D shock evolution model and our measured values of v_b and R_b. The relatively low value of the ambient medium density of ρ_0 of $0.33^{+0.25}_{-0.12}$ amu cm^{-3} is consistent with a lower than average density of the ISM, which could have been produced by the stellar winds of the progenitor sweeping out a cavity in the MC complex and is much lower than the density of molecular H in the clouds surrounding N132D, which range from 10^2 to 10^3 cm^{-3} (H. Sano et al. 2020). For the northeast rim, a density of $0.010^{+0.002}_{-0.001}$ amu cm^{-3} for the $s = 0$ case and $0.007^{+0.001}_{-0.001}$ amu cm^{-3} for the $s = 2$ case match the observed v_b and R_b. These densities are significantly lower than what we derived for the southeastern rim and are consistent with the shock propagating into a low-density medium in the northeast.

An additional constraint is that the northeast region and the southern rim should have the same age since they originated from the same explosion. We calculated model results for the southern rim and northeastern regions for a grid of explosion energies, with energies from $E = 0.5 \times 10^{51}$ erg to 3.0×10^{51} erg in steps of 0.5×10^{51} erg and for ejecta masses ranging from 2 to 10 $M_\odot$ assuming an $s = 0$ ambient medium profile. We found that explosion energies of $1.5–3.0 \times 10^{51}$ erg result in ages of the southern rim and northeastern regions that are consistent with each other and the age from the optical result (C. J. Law et al. 2020), as shown in Figure 12. Ejecta masses of 2−6 $M_\odot$ provide consistent solutions for both regions. Models with explosion energies less than 1.5×10^{51} erg do not provide an age that is consistent with the optical result. The ambient medium densities range from ∼0.33 to 0.66 amu cm^{-3} in the south and ∼0.01–0.02 amu cm^{-3} in the northeast for these solutions. These correspond to estimates of the swept-up mass of ∼22.0–42.5 $M_\odot$.

Table 11
Shock Models for the Southern Rim Region

Parameters	Symbol (Units)	$s = 0$				$s = 2$			
Ejecta mass	M_{ej} ($M_\odot$)	2	4	6	8	2	4	6	8
Reverse shock radius	R_r (pc)	$5.60^{+0.95}_{-2.33}$	$6.88^{+0.31}_{-0.95}$	$7.17^{+0.13}_{-0.49}$	$7.27^{+0.07}_{-0.28}$	$2.30^{+1.97}_{-2.30}$	$4.99^{+0.76}_{-2.03}$	$5.71^{+0.35}_{-1.16}$	$5.98^{+0.16}_{-0.71}$
Age	(yr)	2700^{+790}_{-470}	2860^{+760}_{-440}	3010^{+740}_{-420}	3140^{+710}_{-400}	4190^{+1370}_{-820}	4210^{+1360}_{-810}	4250^{+1340}_{-790}	4290^{+1320}_{-770}

Note. Models for ejecta profile $n = 9$, $R_b = 10.4$ pc, and $v_b = 1620 \pm 400$ km s^{-1} assuming an explosion energy of $E = 1.5 \times 10^{51}$ erg, which corresponds to a circumstellar density (ρ_0) of $0.33^{+0.25}_{-0.12}$ (amu cm^{-3}) and $0.22^{+0.17}_{-0.08}$ (amu cm^{-3}) for the southern rim region for the $s = 0$ and $s = 2$ cases, respectively.

Explosion energies larger than 3.0×10^{51} erg and ejecta masses up to $\sim 9\ M_\odot$ also provide consistent solutions given the relatively large uncertainty on the model ages. Our models cannot rule out such a "hypernova" explanation for N132D but it would be difficult to explain the radius of $R_b = 10.4$ pc, which is in good agreement with the expected size of a stellar-wind bubble created by a $15 \pm 5\ M_\odot$ star. Furthermore, explosion energies larger than 3.0×10^{51} erg are unlikely for normal CCSNe (T. Sukhbold et al. 2016; A. Burrows et al. 2024) and ejecta masses larger than $10\ M_\odot$ are unlikely given that P. Sharda et al. (2020) estimate a progenitor mass of $15 \pm 5\ M_\odot$. We consider the normal CCSNe explanation more likely for N132D.

We also calculated model results for the $s = 2$ profile for explosion energies from $E = 0.5 \times 10^{51}$ erg to 3.0×10^{51} erg in steps of 0.5×10^{51} erg and for ejecta masses ranging from 2 to $10\ M_\odot$ and found that all of these solutions resulted in an age that is discrepant with the optical result. Therefore, a consistent solution for the remnant age can be found for the southern rim and the northeast regions for explosion energies of 1.5–3.0 $\times 10^{51}$ erg and ejecta masses of 2–6 $M_\odot$ for different, but constant density media, in the south and the northeast.

Y. Chen et al. (2003) applied their semianalytic model assuming the thin shell approximation for a shock crossing a density jump to N132D. They adjusted the free parameters in their model (the density contrast at the jump and the evolutionary state of the shock relative to a Sedov solution) to match an age of 3150 yr, an X-ray temperature of $T_x = 0.8$ keV, and an ambient density of $n_o = 3.0$ cm^{-3} to derive an explosion energy of 3.0×10^{51} erg. They suggest that the shock was propagating at 1900 km s^{-1} before encountering the density jump and has decelerated to 800 km s^{-1} in the last 700 yr. Our results agree broadly with their results in that an explosion energy larger than 1.0×10^{51} erg is required to match the data but our measured shock velocity is significantly larger than theirs. We note that they did not consider Coulomb equilibration and adiabatic expansion in their comparison to the X-ray temperature after assuming a shock velocity and they assumed a density jump described by a square wave, which is clearly a simplification.

7. Summary

We have analyzed 878 ks of Chandra data of the LMC SNR N132D from two epochs separated by ≈14.5 yr to measure the expansion of the forward shock. This measurement in X-rays can only be done with the high angular resolution and sensitivity of Chandra. We carry out a comprehensive registration of the pointings using several point-like sources serendipitously detected around the remnant resulting in a relative astrometric precision of 1.8 ± 3.2 mas between the epochs (see Table 3). We extract radial profiles and spectra from 14 narrow regions (∼2.″0) at the rim of the remnant that match the curvature of the shock front. We measure the expansion of the forward shock by comparing intensity profiles between the two epochs (see Section 3) at these 14 locations. We measure an average proper motion of $0.''11 \pm 0.''02$ for eight regions from the bright southern rim and $0.''22 \pm 0.''02$ for two regions in the northeast rim, corresponding to velocities of 1850 ± 390 km s^{-1} and 3630 ± 260 km s^{-1}, respectively. We correct for a bias introduced by the fact that the shape of the Chandra PSF varies with azimuthal angle, which affects comparisons of observations at different azimuthal angles. We also correct for an offset in the adopted COE assuming that the eight southern rim regions have a uniform expansion. After making these corrections, we estimate the shock velocity along the southern rim to be 1620 ± 400 km s^{-1}, and that of the northeast rim to be 3840 ± 260 km s^{-1} (see Figure 7 and Table 9).

We extract and fit spectra from the 14 regions (see Section 4) with a `vpshock` model that provided adequate fits with typical LMC abundances. The fitted electron temperature is $kT_{e,x} = 0.95 \pm 0.17$ keV and $kT_{e,x} = 0.77 \pm 0.04$ keV for the southern rim and northeast rim, respectively. After accounting for Coulomb equilibration and adiabatic expansion the electron temperature for the southern rim is consistent with the temperature one would infer from the measured shock velocity but the electron temperature for the northeast rim is significantly lower than what one would infer from the measured shock velocity. We explore possible explanations for this discrepancy in Section 5, but none of these by themselves can explain the difference. We suggest that this discrepancy warrants further investigation to determine if a combination of effects or effects which we did not consider could explain the discrepancy. We also note that we are limited by the quality of the data and future high angular resolution and high spectral resolution X-ray observations have the potential to resolve the discrepancy. Future missions such as the recently proposed Line Emission Mapper (R. Kraft et al. 2024; S. Orlando et al. 2024) would provide more than an order of magnitude improvement in spectral resolution albeit with worse angular resolution than Chandra, the New Athena mission (M. Cruise et al. 2025) would provide an order of magnitude improvement in effective area and spectral resolution but with worse angular resolution than Chandra, and the Lynx flagship X-ray observatory concept (J. A. Gaskin et al. 2019) would provide more than an order of magnitude improvement in effective area and spectral resolution with comparable angular resolution to Chandra.

We investigate the evolutionary state of the forward shock by comparing our measured shock radii and shock velocities to the 1D SNR models of TM99 assuming the age determined by C. J. Law et al. (2020). We further require that there be a

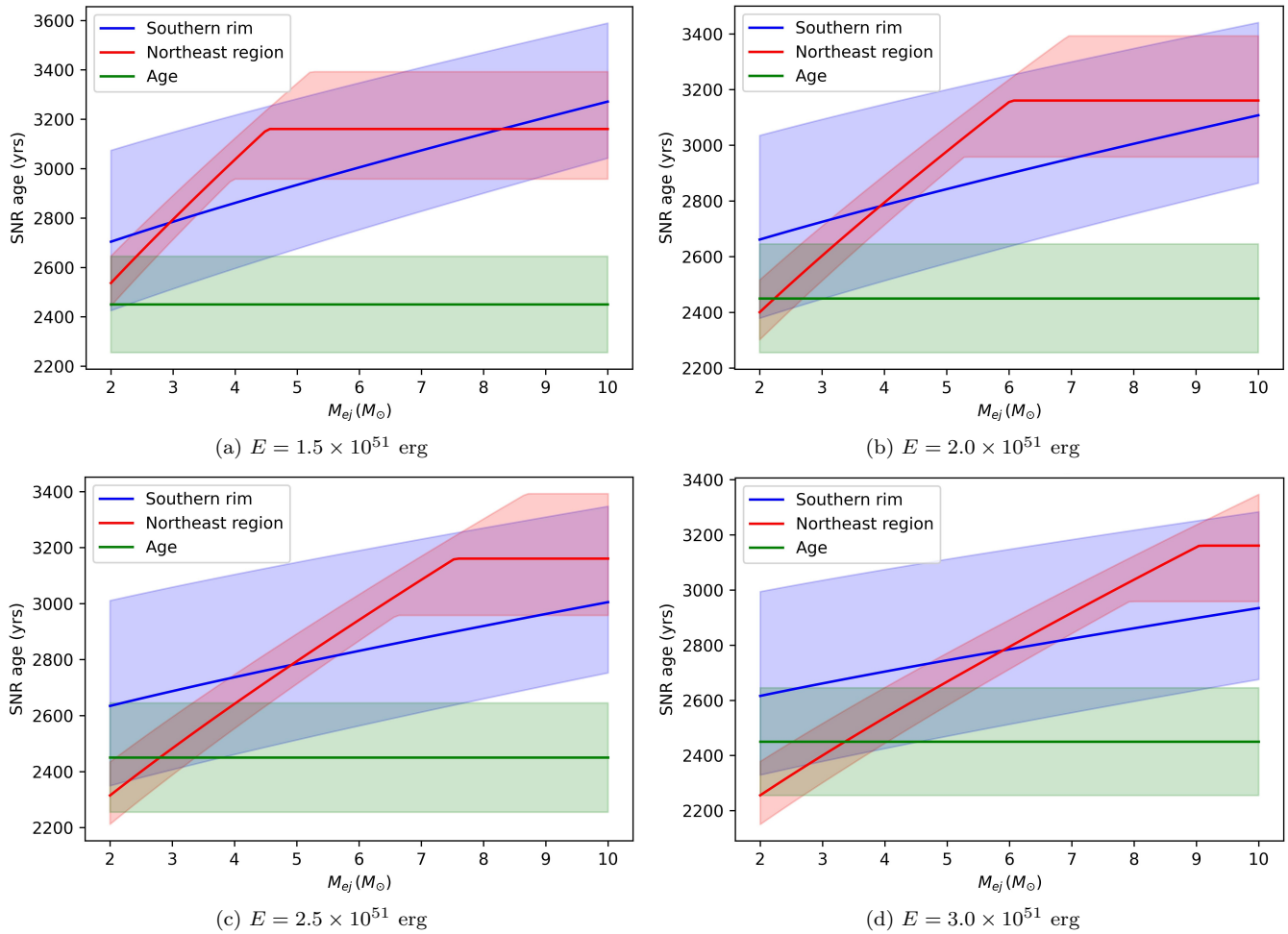

(a) $E = 1.5 \times 10^{51}$ erg (b) $E = 2.0 \times 10^{51}$ erg

(c) $E = 2.5 \times 10^{51}$ erg (d) $E = 3.0 \times 10^{51}$ erg

Figure 12. The 1D model results of the age vs. ejecta mass assuming explosion energies of 1.5–3 $\times$ 10^{51} erg (panels (a)–(d)) and an $s = 0$ ambient medium profile for the southern rim and northeastern regions. The green line and shaded area is the age estimated by C. J. Law et al. (2020) from optical data. The blue and red lines and shaded areas are the results of the 1D model for the southern rim and for the northeastern region respectively.

consistent solution for the southern shock and northeast shock, which have shock velocities and positions that differ by more than a factor of 2. We find consistent solutions for explosion energies of 1.5–3.0 $\times$ 10^{51} erg and ejecta masses of 2–6 $M_\odot$ for a constant ambient medium density of 0.33–0.66 amu cm^{-3} for the southern rim and 0.01–0.02 amu cm^{-3} for the northeast region. Consistent solutions exist for larger values of the explosion energy and ejecta mass, however, we consider these solutions less likely given that the progenitor mass was most likely $15 \pm 5\,M_\odot$ as estimated by P. Sharda et al. (2020) and A. R. Foster et al. (2025). The relatively low and constant value of the ambient density is consistent with the cavity explanation, in which the progenitor created a low-density environment in or around the MC complex to the south. The elongated X-ray morphology to the north and the higher shock velocities in the north are consistent with shock propagation into a low-density medium or a blowout opposite to the MC complex. In summary, the Chandra expansion results are consistent with an energetic SN in a preexisting cavity created by the progenitor.

Acknowledgments

Based on observations with the NASA Chandra X-ray Observatory operated by the Smithsonian Astrophysical Observatory. This work was supported by NASA Chandra X-ray Center grants GO9-20068 and GO2-23045X. P.P.P., T. J.G., V.L.K., and D.J.P. acknowledge support from the Smithsonian Institution and the Chandra X-ray Center through NASA contract NAS8-03060. X.L. is supported by a GRF grant of the Hong Kong Government under HKU 17304524. Support for C.J.L. was provided by NASA through the NASA Hubble Fellowship grant No. HST-HF2-51535.001-A awarded by the Space Telescope Science Institute, which is operated by the Association of Universities for Research in Astronomy, Inc., for NASA, under contract NAS5-26555. D.M. acknowledges support from the National Science Foundation (NSF) through grants PHY-2209451 and AST-2206532.

Facility: NASA Chandra X-ray Observatory (CXO).

Appendix A
Selecting Point Sources for Registration

We carry out spatial registrations of the various observations to each other using point-like sources found serendipitously around the remnant (see Table 2). These sources are primarily selected as having reliable position determinations and for also being present in specific `ObsID` pairs (see the point-source ID column of Table 3).

We estimate the reliability of the position determination by carrying out spatial fits to the data using a ray-traced PSF

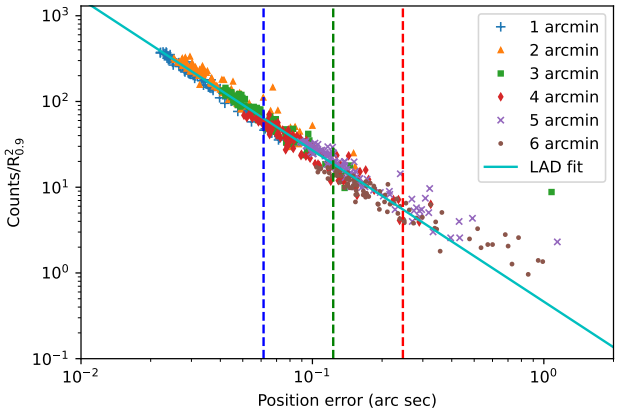

Figure 13. Trend of position errors of spatial fits vs. brightness of simulated point sources. Several point sources are placed at randomly selected azimuthal positions at different off-axis locations (see inset legend for point types corresponding to specific off-axis angles), with counts drawn from a uniform distribution ranging from 5 to 400, and are ray traced, and fitted. The narrow trend is well described by a power law, which we fit using a least absolute deviation (LAD) fit, which is robust to outliers. Vertical dashed lines mark one-eighth, one-quarter, and one-half of the ACIS pixel size to illustrate scale.

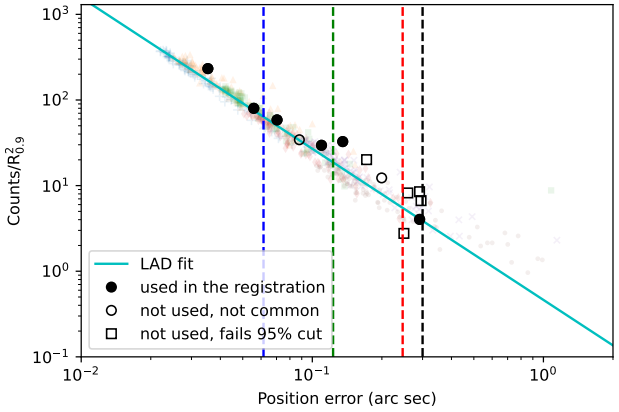

Figure 14. Similar to Figure 13, but an illustration of how sources are selected for registration, using the example of ObsID 21365. Only the detected sources with fitted position errors $< 0.''3$ (rightmost dashed vertical line) are shown. Neither the sources that fall outside the 5%–95% range of the distribution of deviations from the power-law LAD fit (empty squares), nor sources that are not present in other observations (empty circles), are used in the registration. The remaining sources are used for registration (filled circles; see Table 2). All the simulation points from Figure 13 are also shown as gray shaded points. A similar analysis is done for all ObsIDs.

generated separately at each location, and using the position uncertainties as a determining factor for selection for registration. We calibrate the quality of the spatial fitting by carrying out simulations of 100 point sources each at several of f-axis angles ranging from $1'$ to $9'$, which covers the range of all detectable point sources, and fitting their locations for counts ranging from 5 to 400 in each. We add a nominal background to the simulation that corresponds to that seen in ObsID 5532. The results of the fits for the simulated sources are shown in Figure 13, which plots the effective brightness in each simulated source (obtained as the counts from a circular region centered on the best-fit location and within the 90% ECF radius) and its corresponding position error, computed as the square root of the sum of the squared errors along each axis. Note that as is expected, weaker sources have larger position errors. Notice also that the values fall on a narrow locus, which is well fit by a power-law function. The deviations of each point from this fitted power law are a useful diagnostic of the quality of the fit; we consider any source that falls within the 5%–95% range of the distribution of these deviations to be an adequate spatial position fit.

We next identify sources in each observation using wavdetect (P. E. Freeman et al. 2002) and carry out independent spatial fitting, generating a separate ray-traced PSF for each source location. We exclude any source with position error $\geqslant 0.''3$ from further consideration, since deviations larger than that are unlikely according to the aspect astrometric error. This limit is shown for the case of ObsID 21365 in Figure 14 as the rightmost dashed vertical line. From the sample of sources thus selected, we further exclude those which fall outside the 5%–95% bounds of the distribution of deviations (denoted as empty squares in the plot) obtained via simulations. Among the remaining sources (denoted by circular symbols), only those that are also present in other ObsIDs (filled circles) are kept and those that are not (empty circles) are discarded. This method is used for all ObsIDs, and the full list of sources used for registration is listed in Table 2, and the results of the registration based on these sources are in Table 3.

Appendix B
Quantum Efficiency Difference Normalization

We extracted profiles from a $120'' \times 9.''84$ east–west rectangular region in the 1.2–7.0 keV band across the remnant (see Figure 15). The rectangle was split into 732 thin $0.''164 \times 9.''84$ strips. We extracted profiles for the merged Epoch *A* observations; the three Epoch *A* observations were at nearly the same roll. We extracted profiles for the individual Epoch *B* observations. Because observations were at different rolls, the rectangular strip in physical "sky" coordinates covered different regions on the detector depending on the roll. The observations fell into four roll-angle groups (see Table 1 for the roll angles and Figure 16, which shows a representative ObsID from each group). This resulted in three combinations of epoch and node ID: Epoch *A* node 0 and Epoch *B* node 1 (*A*0*B*1), Epoch *A* node 0 and Epoch *B* node 0 (*A*0*B*0), and Epoch *A* node 1 with Epoch *B* node 0 (*A*1*B*0).

To calibrate the QE differences between different nodes and time epochs, we find regions within the rectangle containing only node 0 events or only node 1 events so that the QE for the ⟨epoch⟩⟨node⟩ combinations can be examined (a given region of the remnant that is close to the node boundary can be observed on node 0 and node 1 in an observation because Chandra dithers during observations). Figure 17 displays an example of the distribution of counts between the nodes for the merged Epoch *A* data and one ObsID (21361) from the Epoch *B* data. We accumulated the total scaled counts under the profile for the merged Epoch *A* observations and for each of the Epoch *B* observations. The profiles were corrected for the QE change relative to the reference time as discussed in Section 3. To correct for the exposure time differences, the profiles of the Epoch *A* observations were scaled by a factor $s(t_A) = \tau_{B[j]}/\tau_A$. Here τ_A is the total exposure time for Epoch *A* and $\tau_{B[j]}$ is the exposure for the *j*th observation of Epoch *B*. The ObsIDs for Epoch *B* (and the associated *j* indices) are provided in Table 12. Figure 18 shows the profiles of Epoch *A* observations and one of the Epoch *B* observations (ObsID 21361). The ratio of the accumulated scaled counts between

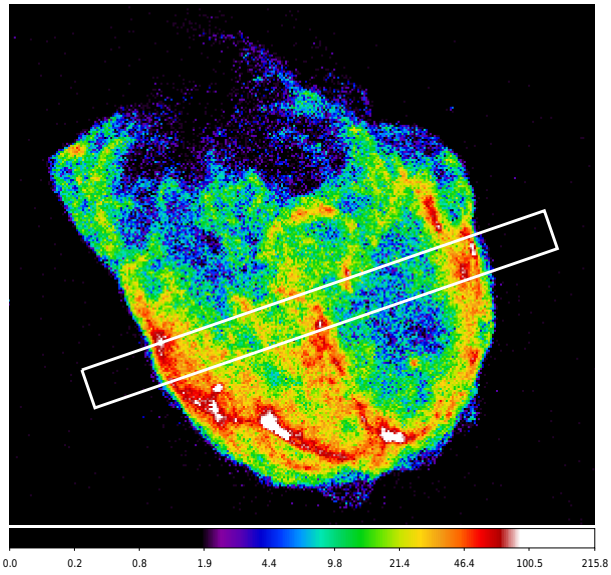

Figure 15. The white rectangle shows the profile extraction region for calculating the initial values of QE difference normalization, plotted on the merged Epoch *A* observations (1.2–7 keV) in ACIS "sky" coordinates.

the green dashed vertical lines and between the orange vertical lines gives the QE difference between the node and epoch combinations. We make the assumption that the intrinsic flux from these regions of the remnant has changed by a negligible amount over the time interval considered.

For example, in Figures 17 and 18, the region between the green vertical dashed lines has scaled counts for Epoch *B*, node 1 (observation *j*) and (merged) Epoch *A*, node 0; the totals of the scaled counts in this region are $C_{B1[j]}$ and C_{A0}. The region between the orange vertical dashed lines has scaled counts for Epoch *B*, node 0 (observation *j*) and Epoch *A*, node 1; the totals of the scaled counts in this region are $C_{B0[j]}$ and C_{A1}. Finally, the region between the black vertical dashed lines has scaled counts for Epoch *B*, node 0 (observation *j*) and (merged) Epoch *A*, node 0; the totals of the scaled counts in this region are $C_{B0[j]}$ and C_{A0}. From these total counts, we can evaluate the relative QEs as $\mathcal{Q}(B1[j];\, A0) = C_{B1[j]}/C_{A0]}$, $\mathcal{Q}(B0[j];\, A1) = C_{B0[j]}/C_{A0]}$, and $\mathcal{Q}(B0[j];\, A0) = C_{B0[j]}/C_{A0]}$. This procedure is carried out for each of the Epoch *B* observations. We list the QE ratios for each Epoch *B* observation in Table 12.

For some Epoch *B* observations, the profile did not have any range with events only from node 1 (observation indices $j = 1$ to 5; see Table 12). We therefore use QE ratios from observations which have data for all three combinations: *B*1*A*0, *B*0*A*0, and *B*0*A*1. The average QE ratios are calculated as averages over the nine observation indices $j = 6$ to 14: $\mathcal{Q}(x;\, y) = (1/9)\sum_{j=6}^{14} \mathcal{Q}(x[j];\, y)$ where *x* and *y* are *B*0, *B*1, or *A*0. The resulting average QE ratios are given in the second part of Table 12.

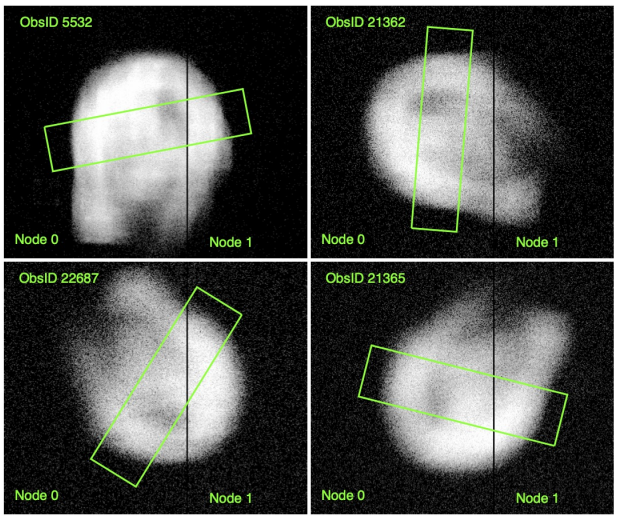

Figure 16. The rectangular profile extraction regions in detector coordinates (CHIPX, CHIPY) for representative ObsIDs from each of the four roll groups. The upper left panel corresponds to Epoch *A*. The remaining panels show the Epoch *B* groups.

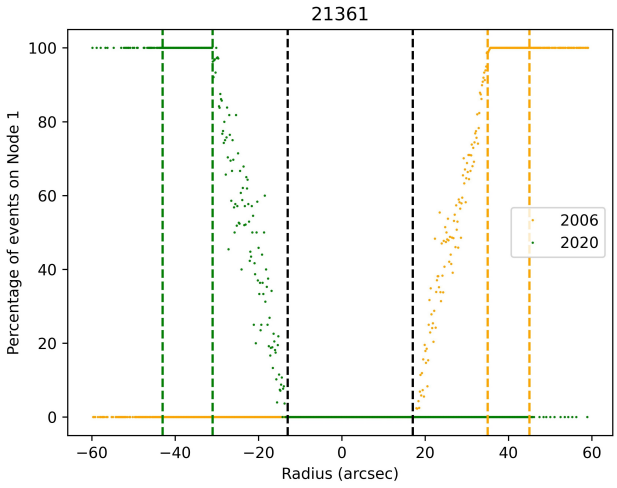

Figure 17. The percentage of events on node 1 for Epoch *A* observations (2006) and one of the Epoch *B* observations (ObsID 21361, 2020). The range between green dashed lines has events combination *A*0*B*1, the range between black dashed lines has events combination *A*0*B*0, and the range between orange dashed lines has events combination *A*1*B*0.

To correct the QE difference to the same level, we chose the averaged node 0, Epoch *B* as the reference. The QE difference normalizations from the rectangle region were used to scale the weight for each event according to the node ID and epoch. The correction factors range from ∼3% to ∼7% indicating that the QE is lower in Epoch *B* than the current calibration files estimate.

Table 12
Quantum Efficiency Ratio between Node 0 and Node 1 at Different Epochs, and Quantum Efficiency Ratios Averaged over $j = 6$ to 14

ObsID (j)	Roll	$\mathcal{Q}(B1[j]; A0)$	$\mathcal{Q}(B0[j]; A0)$	$\mathcal{Q}(B0[j]; A1)$
21362 (1)	255.62	⋯	0.956 ± 0.017	0.892 ± 0.024
22094 (2)	93.15	⋯	0.900 ± 0.040	0.897 ± 0.023
22841 (3)	93.15	⋯	0.927 ± 0.041	0.908 ± 0.023
22687 (4)	102.66	⋯	0.923 ± 0.042	0.887 ± 0.023
21363 (5)	105.15	⋯	0.956 ± 0.021	0.904 ± 0.021
21361 (6)	160.14	0.956 ± 0.021	1.000 ± 0.020	0.930 ± 0.026
23317 (7)	160.14	0.952 ± 0.021	0.967 ± 0.019	0.920 ± 0.022
21365 (8)	175.14	0.966 ± 0.018	0.974 ± 0.016	0.960 ± 0.019
21884 (9)	183.14	0.971 ± 0.026	0.949 ± 0.019	0.931 ± 0.022
23044 (10)	175.15	0.946 ± 0.019	0.965 ± 0.016	0.950 ± 0.020
21886 (11)	175.14	0.983 ± 0.021	0.963 ± 0.018	0.910 ± 0.021
21883 (12)	178.14	0.947 ± 0.019	0.952 ± 0.021	0.931 ± 0.025
21882 (13)	178.14	0.999 ± 0.020	0.988 ± 0.020	0.919 ± 0.024
21887 (14)	183.14	0.962 ± 0.019	0.950 ± 0.016	0.907 ± 0.020
		$\mathcal{Q}(B1; A0)$	$\mathcal{Q}(B0; A0)$	$\mathcal{Q}(B0; A1)$
Average ($j = 6.14$)		0.964 ± 0.007	0.967 ± 0.006	0.929 ± 0.007

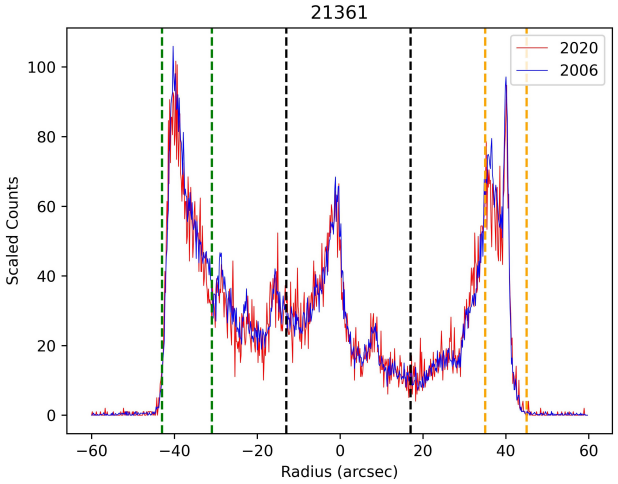

Figure 18. The QE and exposure time corrected profiles from Epoch *A* observations (2006) and one of the Epoch *B* observations (ObsID 21361, 2020). The range between green dashed lines has the events combination *A*0*B*1, the range between black dashed lines has the events combination *A*0*B*0, and the range between orange dashed lines has the events combination *A*1*B*0.

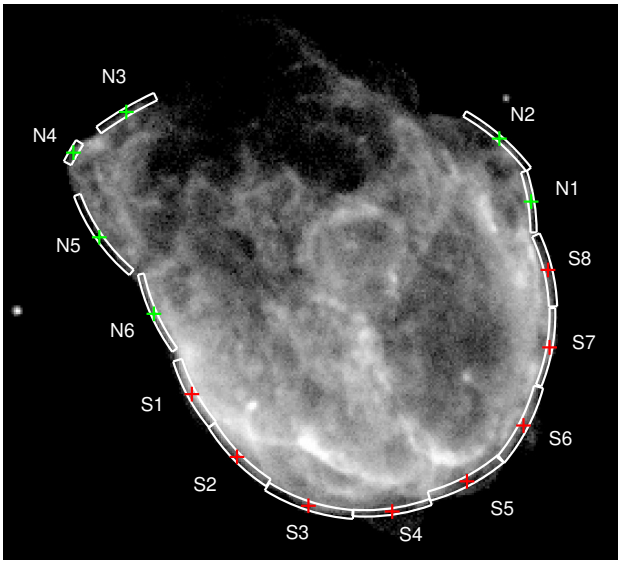

Figure 19. The positions for the PSF simulations for the S1–S8 and N1–N6 regions. The red and green crosses are the PSF simulation centers and match the region color coding in Figure 20. The white sectors are the shock regions where we measure the expansion (see Table 5).

Appendix C
Accounting for Point-spread Function and Center of Explosion Bias

Based on PSF simulations, we find that differences in the PSF as a function of off-axis and azimuthal angle between the Epoch *A* and Epoch *B* observations could result in an apparent "shift" of the forward shock. This is the result of the same region of the remnant being observed at different azimuthal angles in Epoch *A* and Epoch *B*. Given the small range in of f-axis angles (less than 1.′0) of the regions considered in this analysis, the variation in azimuthal angle is the dominant effect. We investigate these systematics by using SAOTrace and MARX to simulate PSFs at the centers of the shock regions as shown in Figure 19. The simulated PSFs were convolved with a 2D theoretical shock model, based on a line-of-sight projection through a spherical rim "cap," to simulate the observed shock front. We extracted a radial profile in the 1.2–7 keV passband of simulated nonmoving shock fronts using the merged Epoch *A* and merged Epoch *B* event lists based on the PSF simulations separately, then measured the apparent displacements in the shock profiles using the same method described in Section 3. The "expansions" resulting from the PSF bias are shown in Figure 20, displaying a sinusoidal-type behavior with region orientation angle. Such a sinusoidal behavior with azimuthal angle is expected given the PSF aberration of the Chandra mirrors, and we therefore fit these data with a sinusoid to determine the bias as a function of angle. To correct the expansion for PSF bias, we subtract the fitted model values shown in Figure 20 from the raw shifts shown in Figure 6 to obtain the PSF-bias-corrected expansion in Figure 21.

We also explore the possibility that our assumed COE introduces a bias in our expansion measurement. Under the assumption that the southern rim is expanding uniformly, any error in the assumed COE would introduce residuals with a

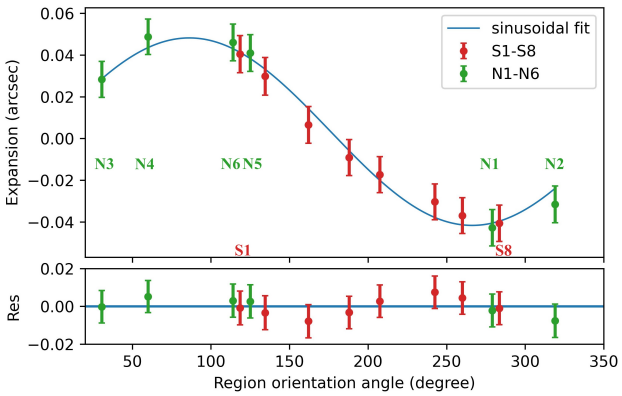

Figure 20. Estimate of the systematic bias in the expansion measurement due to PSF differences. The data points are arranged similarly to Figure 6 with regions S1–S8 labeled sequentially from left to right. The apparent expansion derived from PSF simulations with the appropriate off-axis and azimuthal angles of the Epoch *A* and Epoch *B* observations of a nonmoving shock front at the locations marked in Figure 19 are shown, along with the sinusoidal fit (solid blue line) to all the points. This sinusoidal variation is attributable to the PSF bias.

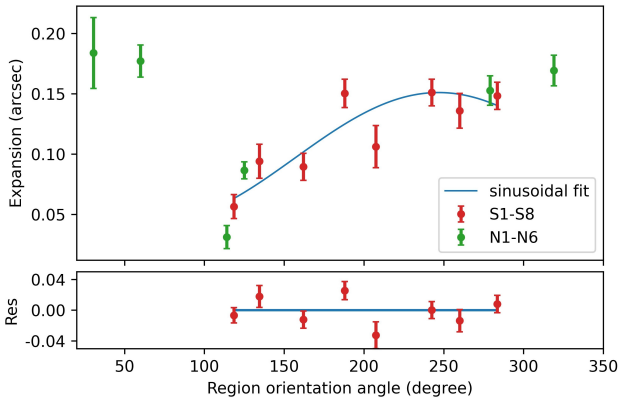

Figure 21. Estimate of the systematic bias in the expansion measurement due to an error in the assumed COE. The apparent expansion from Figure 20 is subtracted from the measured raw expansion shown in Figure 6, and a sinusoid is fit to account for an offset in the assumed expansion center (see Equation (C1); solid blue line). The final estimate of the expansion in Figure 7 accounts for this offset.

sinusoidal pattern. If that is the case, a correction to the expansion center can be obtained by fitting the eight southern regions with a sinusoid (equivalent to an offset eccentric circle):

$$\delta R_n = \Delta X \sin\theta_n - \Delta Y \cos\theta_n + \Delta R_S, \qquad \text{(C1)}$$

where δR_n is the expansion of each of the southern regions (corrected for the PSF bias effect; see Figure 21), and θ_n are the region orientation angles (see Table 5). The parameters ΔX and ΔY define the shift of the COE in the R.A. and decl. directions, respectively, and ΔR_S defines the average expansion of the southern regions. Fitting such a model to the data in Figure 21 results in a shift in R.A. of $\Delta X = -0\farcs05 \pm 0\farcs007$ and in decl. of $\Delta Y = 0\farcs02 \pm 0\farcs012$, with $\Delta R_S = 0\farcs097 \pm 0\farcs008$. The COE given in Table 7 includes the corrections (ΔX, ΔY). We provide a conservative assessment of the errors on ΔR_S in Table 6 accounting for the uncertainty in the estimates of each δR_n as well as the scatter therein. The COE correction is applied to each of the regions in Figure 21 as $\Delta X \sin\theta_n - \Delta Y \cos\theta_n$, and the result is shown in Figure 7.

ORCID iDs

Xi Long https://orcid.org/0000-0003-3350-1832
Paul P. Plucinsky https://orcid.org/0000-0003-1415-5823
Terrance J. Gaetz https://orcid.org/0000-0002-5115-1533
Vinay L. Kashyap https://orcid.org/0000-0002-3869-7996
Aya Bamba https://orcid.org/0000-0003-0890-4920
William P. Blair https://orcid.org/0000-0003-2379-6518
Daniel Castro https://orcid.org/0000-0002-0394-3173
Adam R. Foster https://orcid.org/0000-0003-3462-8886
Charles J. Law https://orcid.org/0000-0003-1413-1776
Dan Milisavljevic https://orcid.org/0000-0002-0763-3885
Eric Miller https://orcid.org/0000-0002-3031-2326
Daniel J. Patnaude https://orcid.org/0000-0002-7507-8115
Manami Sasaki https://orcid.org/0000-0001-5302-1866
Hidetoshi Sano https://orcid.org/0000-0003-2062-5692
Piyush Sharda https://orcid.org/0000-0003-3347-7094
Benjamin F. Williams https://orcid.org/0000-0002-7502-0597
Brian J. Williams https://orcid.org/0000-0003-2063-381X
Hiroya Yamaguchi https://orcid.org/0000-0002-5092-6085

References

Ackermann, M., Albert, A., Atwood, W. B., et al. 2016, A&A, 586, A71
Allen, G. E., Houck, J. C., & Sturner, S. J. 2008, ApJ, 683, 773
Arnaud, K. A. 1996, in ASP Conf. Ser. 101, Astronomical Data Analysis Software and Systems V, ed. G. H. Jacoby & J. Barnes (San Francisco, CA: ASP), 17
Bamba, A., Ohira, Y., Yamazaki, R., et al. 2018, ApJ, 854, 71
Banas, K. R., Hughes, J. P., Bronfman, L., & Nyman, L. Å. 1997, ApJ, 480, 607
Banovetz, J., Milisavljevic, D., Sravan, N., et al. 2023, ApJ, 948, 33
Bhalerao, J., Park, S., Schenck, A., Post, S., & Hughes, J. P. 2019, ApJ, 872, 31
Blair, W. P., Morse, J. A., Raymond, J. C., et al. 2000, ApJ, 537, 667
Borkowski, K. J., Lyerly, W. J., & Reynolds, S. P. 2001, ApJ, 548, 820
Borkowski, K. J., Hendrick, S. P., & Reynolds, S. P. 2007, ApJ, 671, L45
Borkowski, K. J., Gwynne, P., Reynolds, S. P., et al. 2017, ApJL, 837, L7
Burkhart, B. 2018, ApJ, 863, 118
Burrows, A., Wang, T., & Vartanyan, D. 2024, ApJL, 964, L16
Cantat-Gaudin, T. 2022, Univ, 8, 111
Cash, W. 1979, ApJ, 228, 939
Chen, Y., Zhang, F., Williams, R. M., & Wang, Q. D. 2003, ApJ, 595, 227
Chen, Y., Zhou, P., & Chu, Y.-H. 2013, ApJL, 769, L16
Chevalier, R. A. 1999, ApJ, 511, 798
Chevalier, R. A., & Liang, E. P. 1989, ApJ, 344, 332
Chevalier, R. A., & Fransson, C. 1994, ApJ, 420, 268
Clementini, G., Gratton, R., Bragaglia, A., et al. 2003, AJ, 125, 1309
Cox, D. P., & Smith, B. W. 1974, ApJ, 189, L105
Cruise, M., Guainazzi, M., Aird, J., et al. 2025, NatAs, 9, 36
Danziger, I. J., & Dennefeld, M. 1976, ApJ, 207, 394
de Avillez, M., & Breitschwerdt, D. 2004, Ap&SS, 292, 207
Decourchelle, A., Ellison, D. C., & Ballet, J. 2000, ApJ, 543, L57
Dopita, M. A., Vogt, F. P. A., Sutherland, R. S., et al. 2018, ApJS, 237, 10
Dwarkadas, V. V. 2005, ApJ, 630, 892
Dwarkadas, V. V. 2007, ApJ, 667, 226
Dwarkadas, V. V. 2023, Galax, 11, 78
El-Badry, K., Ostriker, E. C., Kim, C.-G., Quataert, E., & Weisz, D. R. 2019, MNRAS, 490, 1961
Ellison, D. C., Patnaude, D. J., Slane, P., Blasi, P., & Gabici, S. 2007, ApJ, 661, 879
Favata, F., Vink, J., Parmar, A. N., Kaastra, J. S., & Mineo, T. 1997, A&A, 324, L45
Foster, A. R., Plucinsky, P. P., Gaetz, T. J., Long, X., & Jerius, D. 2025, ApJ, 986, 8
Freeman, P. E., Kashyap, V., Rosner, R., & Lamb, D. Q. 2002, ApJS, 138, 185
Fruscione, A., McDowell, J. C., Allen, G. E., et al. 2006, Proc. SPIE, 6270, 62701V
Gaskin, J. A., Swartz, D. A., Vikhlinin, A., et al. 2019, JATIS, 5, 021001
Gent, F. A., Shukurov, A., Fletcher, A., Sarson, G. R., & Mantere, M. J. 2013, MNRAS, 432, 1396
H. E. S. S. Collaboration, Abdalla, H., Aharonian, F., et al. 2021, A&A, 655, A7

Heger, A., Fryer, C. L., Woosley, S. E., Langer, N., & Hartmann, D. H. 2003, ApJ, 591, 288
Helder, E. A., Vink, J., Bykov, A. M., et al. 2012, SSRv, 173, 369
HI4PI Collaboration, Ben Bekhti, N., Flöer, L., et al. 2016, A&A, 594, A116
Houck, J. C., & Allen, G. E. 2006, ApJS, 167, 26
Hughes, J. P. 1987, ApJ, 314, 103
Hughes, J. P., Hayashi, I., & Koyama, K. 1998, ApJ, 505, 732
Hughes, J. P., Rakowski, C. E., Burrows, D. N., & Slane, P. O. 2000, ApJ, 528, L109
Hwang, U., & Laming, J. M. 2003, ApJ, 597, 362
Hwang, U., & Laming, J. M. 2012, ApJ, 746, 130
Joung, M. K. R., & Mac Low, M.-M. 2006, ApJ, 653, 1266
Kim, C.-G., & Ostriker, E. C. 2015, ApJ, 802, 99
Kim, C.-G., & Ostriker, E. C. 2017, ApJ, 846, 133
Kobayashi, C., Umeda, H., Nomoto, K., Tominaga, N., & Ohkubo, T. 2006, ApJ, 653, 1145
Kraft, R., Bogdán, Á., ZuHone, J., et al. 2024, Proc. SPIE, 13093, 1309327
Laming, J. M., & Hwang, U. 2003, ApJ, 597, 347
Lasker, B. M. 1978, ApJ, 223, 109
Lasker, B. M. 1980, ApJ, 237, 765
Law, C. J., Milisavljevic, D., Patnaude, D. J., et al. 2020, ApJ, 894, 73
Lee, H., Kashyap, V. L., van Dyk, D. A., et al. 2011, ApJ, 731, 126
McKee, C. F., & Ostriker, J. P. 1977, ApJ, 218, 148
McKee, C. F., van Buren, D., & Lazareff, B. 1984, ApJ, 278, L115
Micelotta, E. R., Dwek, E., & Slavin, J. D. 2016, A&A, 590, A65
Morse, J. A., Winkler, P. F., & Kirshner, R. P. 1995, AJ, 109, 2104
Morse, J. A., Blair, W. P., Dopita, M. A., et al. 1996, AJ, 112, 2350
Motte, F., Bontemps, S., & Louvet, F. 2018, ARA&A, 56, 41
Nomoto, K., Kobayashi, C., & Tominaga, N. 2013, ARA&A, 51, 457
Nomoto, K., Tominaga, N., Umeda, H., Kobayashi, C., & Maeda, K. 2006, NuPhA, 777, 424
Oey, M. S. 1996, ApJ, 467, 666
Ohshiro, Y., Suzuki, S., Okada, Y., Suzuki, H., & Yamaguchi, H. 2024, ApJ, 976, 180
Okada, Y., Ohshiro, Y., Suzuki, S., et al. 2025, ApJ, 982, 190
Orlando, S., Miceli, M., Patnaude, D. J., et al. 2024, arXiv:2408.12462
Padoan, P., & Nordlund, Å. 2011, ApJ, 730, 40
Patnaude, D. J., & Fesen, R. A. 2003, ApJ, 587, 221
Patnaude, D. J., Ellison, D. C., & Slane, P. 2009, ApJ, 696, 1956
Patnaude, D. J., Lee, S.-H., Slane, P. O., et al. 2015, ApJ, 803, 101
Pfalzner, S., Kaczmarek, T., & Olczak, C. 2012, A&A, 545, A122
Pietrzyński, G., Graczyk, D., Gieren, W., et al. 2013, Natur, 495, 76
Pietrzyński, G., Graczyk, D., Gallenne, A., et al. 2019, Natur, 567, 200
Plucinsky, P. P., Bogdan, A., Germain, G., & Marshall, H. L. 2016, Proc. SPIE, 9905, 990544
Plucinsky, P. P., Bogdan, A., & Marshall, H. L. 2022, Proc. SPIE, 12181, 121816X
Raymond, J. C., Ghavamian, P., Bohdan, A., et al. 2023, ApJ, 949, 50
Sano, H., Fukui, Y., Yoshiike, S., et al. 2015, in ASP Conf. Ser. 499, Revolution in Astronomy with ALMA: The Third Year, ed. D. Iono et al. (San Francisco, CA: ASP), 257
Sano, H., Fujii, K., Yamane, Y., et al. 2017, in AIP Conf. Proc. 1792, 6th Int. Symp. on High Energy Gamma-Ray Astronomy (Melville, NY: AIP), 040038
Sano, H., Plucinsky, P. P., Bamba, A., et al. 2020, ApJ, 902, 53
Sedov, L. I. 2018, Similarity and Dimensional Methods in Mechanics (10th ed.; Boca Raton, FL: CRC Press)
Sharda, P., Gaetz, T. J., Kashyap, V. L., & Plucinsky, P. P. 2020, ApJ, 894, 145
Shimoda, J., Inoue, T., Ohira, Y., et al. 2015, ApJ, 803, 98
Silich, S., Tenorio-Tagle, G., & Añorve-Zeferino, G. A. 2005, ApJ, 635, 1116
Slane, P., Bykov, A., Ellison, D. C., Dubner, G., & Castro, D. 2016, in Multi-scale Structure Formation and Dynamics in Cosmic Plasmas, ed. A. Balogh et al., Vol. 51 (New York: Springer), 187
Sukhbold, T., Ertl, T., Woosley, S. E., Brown, J. M., & Janka, H.-T. 2016, ApJ, 821, 38
Sutherland, R. S., & Dopita, M. A. 1995, ApJ, 439, 365
Suzuki, H., Plucinsky, P. P., Gaetz, T. J., & Bamba, A. 2021, A&A, 655, A116
Tenorio-Tagle, G., Bodenheimer, P., Franco, J., & Rozyczka, M. 1990, MNRAS, 244, 563
Tenorio-Tagle, G., Rozyczka, M., Franco, J., & Bodenheimer, P. 1991, MNRAS, 251, 318
Truelove, J. K., & McKee, C. F. 1999, ApJS, 120, 299
Truelove, J. K., & McKee, C. F. 2000, ApJS, 128, 403
Verner, D. A., & Yakovlev, D. G. 1995, A&AS, 109, 125
Vink, J., Patnaude, D. J., & Castro, D. 2022a, ApJ, 929, 57
Vink, J., Rachel, S., Nukri, K., & Dmitry, P. 2022b, ICRC Berlin, 37, 778
Virtanen, P., Gommers, R., Oliphant, T. E., et al. 2020, NatMe, 17, 261
Vogt, F., & Dopita, M. A. 2011, Ap&SS, 331, 521
Ward, J. L., & Kruijssen, J. M. D. 2018, MNRAS, 475, 5659
Westerlund, B. E., & Mathewson, D. S. 1966, MNRAS, 131, 371
Williams, B. J., Borkowski, K. J., Reynolds, S. P., et al. 2006, ApJ, 652, L33
Williams, B. J., Blair, W. P., Borkowski, K. J., et al. 2018, ApJL, 865, L13
Wilms, J., Allen, A., & McCray, R. 2000, ApJ, 542, 914
Wright, N. J. 2020, NewAR, 90, 101549
Xi, L., Gaetz, T. J., Plucinsky, P. P., Hughes, J. P., & Patnaude, D. J. 2019, ApJ, 874, 14
Xiao, X., & Chen, Y. 2008, AdSpR, 41, 416
XRISM Collaboration, Audard, M., Awaki, H., et al. 2024, PASJ, 76, 1186
Zinnecker, H., & Yorke, H. W. 2007, ARA&A, 45, 481